# A phase-field fracture formulation for generalized standard materials: The interplay between thermomechanics and damage

Svolos, Lampros
Tran, Quoc-Thai
Djibrilla Boureima, Ismael
Anghel, Veronica
Garikipati, Krishna
Mourad, Hashem Mohamed



**To be published in:** Journal of the Mechanics and Physics of Solids

**DOI to publisher's version:** 10.1016/j.jmps.2025.106154

# Journal Pre-proof


A phase-field fracture formulation for generalized standard materials: The interplay between thermomechanics and damage

Lampros Svolos, Quoc-Thai Tran, Ismael D. Boureima,
Veronica Anghel, Krishna Garikipati, Hashem M. Mourad

PII: S0022-5096(25)00130-9
DOI: https://doi.org/10.1016/j.jmps.2025.106154
Reference: MPS 106154

To appear in: *Journal of the Mechanics and Physics of Solids*

Received date : 12 October 2024
Revised date : 13 April 2025
Accepted date : 14 April 2025

Please cite this article as: L. Svolos, Q.-T. Tran, I.D. Boureima et al., A phase-field fracture formulation for generalized standard materials: The interplay between thermomechanics and damage. *Journal of the Mechanics and Physics of Solids* (2025), doi: https://doi.org/10.1016/j.jmps.2025.106154.

# A phase-field fracture formulation for generalized standard materials: The interplay between thermomechanics and damage

Lampros Svolos[a,*], Quoc-Thai Tran[b], Ismael D. Boureima[b], Veronica Anghel[c], Krishna Garikipati[d], Hashem M. Mourad[b]

[a] *Department of Civil and Environmental Engineering, University of Vermont, Burlington, VT, USA*
[b] *Theoretical Division, Los Alamos National Laboratory, Los Alamos, NM, USA*
[c] *Materials Science and Technology Division, Los Alamos National Laboratory, Los Alamos, NM, USA*
[d] *Department of Aerospace and Mechanical Engineering, University of Southern California, Los Angeles, CA, USA*

**Abstract**

Accurately modeling fracture of ductile materials poses open challenges in the field of computational mechanics due to the multiphysics nature of their failure processes. Integrating the interplay between thermodynamics and damage into ductile fracture models is vital for predicting critical failure modes. In this paper, we develop a versatile phase-field (PF) framework for modeling ductile fracture, taking into account finite-strain elasto-plasticity. The framework stems from a variational formulation of constitutive relations for generalized standard materials (GSMs), whose response is described by a Helmholtz free energy and a dissipation pseudo-potential. Its variational structure is based on a minimum principle for a functional that expresses the sum of power densities for reversible and irreversible processes. By minimizing this functional with a constraint on a von Mises yield function, we derive the evolution equation for the equivalent plastic strain and an associative flow rule. This constrained optimization problem is analytically solved for a wide class of thermo-viscoplasticity models. The key innovations of the current work include (i) a cubic plastic degradation function that accounts for a non-vanishing damage-dependent yield stress, (ii) closed-form expressions of the Helmholtz free energy and dissipation pseudo-potential for three thermo-viscoplasticity models, (iii) an extended Johnson-Cook plasticity model with a nonlinear hardening law, and (iv) a plastic work heat source that depends on the plastic degradation function and a variable Taylor-Quinney (TQ) coefficient. The capabilities of the proposed framework are tested with the aid of four ductile fracture problems, including the Sandia Fracture Challenge. In each of these problems, we examine the evolution of relevant field variables such as the PF order parameter, the equivalent plastic strain, the temperature, and the internal power dissipation density, in addition to the overall structural response quantified by the force–displacement curve. These numerical studies demonstrate that the proposed framework effectively represents ductile fracture, yielding computational results that exhibit good agreement with experimental data.

*Keywords:* Ductile fracture, Phase-field modeling, Generalized standard materials, Thermo-viscoplasticity

## 1. Introduction

Ductility is an important mechanical property of materials in applications where metallic structures are subjected to dynamic/impact loading. Extensive plastic deformation may be a desirable mechanical response in many applications,

*Corresponding author
*Email address:* Lampros.Svolos@uvm.edu (Lampros Svolos)

such as energy absorbers and protective barriers, as it helps reduce internal forces transferred within a structure and prevent abrupt failure. The need to reliably adopt ductile materials in design standards motivates efforts aimed at developing predictive models capable of capturing their inelastic and failure behaviors. Despite considerable investigation conducted over the past few decades, accurately modeling ductile fracture continues to pose open challenges in the field of solid mechanics [1–3].

The plastic behavior of ductile materials typically depends on state variables such as temperature, as well as loading conditions and history. These dependencies play a critical role in determining the behavior of such materials, especially under extreme loading conditions. In addition, in such materials there is a two-way coupling between mechanical and thermal effects. For example, temperature rise typically leads to thermal softening, i.e. a decrease in the plastic flow stress. It is also widely accepted that a significant portion of the plastic work, $\sim 90\%$ as quantified by the Taylor-Quinney (TQ) coefficient, is converted into heat during the inelastic deformation of metallic materials [4, 5]. Given these facts, it is clear that accurately representing the dynamic plastic response of metals requires the development of constitutive relations that account for thermomechanical coupling, and various material models [6–10] capture such factors via mechanistic or (semi-)empirical expressions for the plastic flow stress $\sigma_y$.

The concept of generalized standard materials (GSM) was first introduced by Halphen and Nguyen [11] to express state and evolution equations (e.g., changes in hardening parameters over time) based on the variation of a single functional. This variational framework facilitates the development of thermodynamically consistent constitutive models using finite-strain elastoplasticity theory [12, 13]. In this framework, the response of GSMs in solids is described by a Helmholtz free energy and a dissipation pseudo-potential [14], expressed as functions of state variables. The local constitutive model is recast into an optimization problem using the aforementioned energies. This approach gives rise to the evolution equations for the internal variables and provides a generic formulation of flow laws [15, 16]. This theoretical treatment of constitutive modeling plays a critical role in the area of phenomenological material modeling because it circumvents oft-encountered problems in finite-strain elastoplasticity related to the arbitrariness of yield functions and flow rules [17]. More recently, it has been applied to coupled thermomechanical dissipative systems [18–20].

The foundation of the field of fracture mechanics can be traced back to the seminal work of Griffith [21, 22] on brittle materials. Interpreting crack propagation as a competition between the surface energy due to crack formation and the linear elastic energy stored in brittle materials was revolutionary, leading to an energy-based description of crack growth [23]. However, the non-physical assumption of linear elastic mechanical behavior (e.g., resulting in infinite stresses at crack tips) was originally highlighted by Irwin [24], as experimental observations confirmed the occurrence of plastic deformation at crack fronts (even in materials considered as brittle) [25, 26]. Hence, the surface energy in Griffith's theory was modified to account for the plastic work as dissipative energy in ductile materials.

Phase-field (PF) modeling of fracture offers a comprehensive framework for simulating crack initiation and propagation in materials. The PF approach to fracture was first introduced by Bourdin et al. [27] as a numerical approximation of the variational model of crack evolution aligned with Griffith's theory [28]. Within this framework, the solution to a fracture problem is determined by minimizing the total potential energy of a solid body, which is the summation of the bulk elastic energy and crack surface energy. To obtain a regularized representation of cracks, PF models

introduce an auxiliary field, denoted herein by $d$, and its gradient. Higher-order spatial derivatives can potentially be included, which were treated by continuous-discontinuous Galerkin methods in [29]. These models are remarkably similar to gradient-enhanced continuum damage models [30], which were also treated by continuous-discontinuous Galerkin methods [31, 32].

Over recent decades, the PF fracture approach has gained significant attention in the computational mechanics community due to its effectiveness in capturing complex fracture patterns (e.g., crack merging and branching), which have proved challenging to finite element methods based on discontinuity-resolving formulations [33]. Miehe et al. [34] introduced a pivotal PF framework for modeling brittle fracture based on gradient-damage theory and thermodynamic principles. This framework was extended to address dynamic brittle fracture in [35, 36]. Additional developments of the PF approach successfully represented cohesive fracture, as demonstrated in [37–39]. Furthermore, thermodynamically consistent PF frameworks were presented in [40–42] to represent ductile fracture by coupling plasticity with gradient damage, since the Griffith-type variational theory that describes the brittle fracture process does not apply directly to the ductile case [43]. It is also generally recognized that the ability to accurately predict the behavior of ductile materials at/near failure requires an adequate representation of the interplay between thermomechanics and damage, since fracture is ultimately observed in ductile materials after (sometimes extensive) plastic deformation. It is therefore important to note that, when coupled with viscoplastic constitutive laws, thermodynamically consistent PF models have been shown to capture shear band formation—a precursor to ductile fracture, e.g. see [44, 45]. More recent research efforts also explored the interaction between damage and heat transfer in both brittle [46, 47] and ductile materials [48, 49].

In the present paper, we develop a phase-field framework for modeling ductile fracture within finite-strain elasto-plasticity using the variational formulation of constitutive relations for generalized standard materials. Inspired by the work of Ortiz and Stainier [12], we adopt a minimum principle for a functional that expresses the sum of power densities. By applying the second law of thermodynamics and minimizing this functional with a constraint on the von Mises yield function, we find the evolution equation for the equivalent plastic strain and the standard associative $J_2$ flow rule. This constrained optimization problem is analytically solved for a broad class of thermo-viscoplasticity models with flow-stress expressions that can be decomposed multiplicatively. The latter approach is novel and provides a versatile framework to couple PF fracture with such models (e.g., Johnson-Cook and a modified Zerilli-Armstrong models). In addition, we propose (i) a cubic plastic degradation function to account for the non-vanishing values of the damage-dependent yield stress, (ii) an extended Johnson-Cook (XJC) plasticity model with a nonlinear hardening law, and (iii) a plastic work heat source that depends on the plastic degradation function and a variable TQ coefficient. The modeling capabilities of the proposed phase-field (PF) framework are tested with the aid of benchmark problems of ductile fracture using different thermo-viscoplasticity models. Its performance is assessed by comparing numerical results against experimental data from the Sandia Fracture Challenge [1].

The remainder of this paper is organized as follows. In Section 2, we briefly present kinematic relationships and conservation laws required for the derivation of the governing equations used to determine the unknown fields; namely, the displacement, temperature, and phase field. The variational formulation of constitutive relations for generalized standard materials is described in detail in Section 3. This includes the statement of the minimum principle in terms

of the total dissipation density, the imposition of the second law of thermodynamics in the form of the Clausius-Duhem inequality, and the derivation of the flow rule from the aforementioned constrained optimization problem. In Section 4, we propose a versatile PF framework for ductile fracture, which can be used with a broad class of thermo-viscoplasticity models, and we specify the different terms appearing in the Helmholtz free energy expression. Numerical examples involving four benchmark problems of ductile fracture are presented in Section 5 to assess the modeling and predictive capabilities of the proposed framework. Notably, we compare our numerical results to experimental data from the Sandia Fracture Challenge, and present sensitivity analyses examining the influence of the plastic degradation function on the load-bearing capacity of the structures under consideration. Finally, a summary and conclusions are presented in Section 6.

### *1.1. Notation: Symbols and operations*

In this work, tensors and vectors are denoted by italicized boldface letters, while fourth-order tensors are distinguished by a blackboard bold typeface style (e.g., the elasticity tensor $\mathbb{C}$). The dot product of two vectors $\boldsymbol{v}$ and $\boldsymbol{w}$ is given by $\boldsymbol{v}\cdot\boldsymbol{w} = v_i w_i$, where the summation is implied over repeated indices (i.e., the Einstein summation convention). The double contraction between two second-order tensors $\boldsymbol{A}$ and $\boldsymbol{B}$ is defined as $\boldsymbol{A} : \boldsymbol{B} = A_{ij}B_{ij}$, where the indices $i$ and $j$ follow the Einstein summation convention. The dot operator is omitted for scalar products unless it is used for the sake of clarity. The symbol $\dot{x}$ (i.e., over-dot) denotes the time derivative of the quantity $x$ (scalar or tensor). The single contraction of second-order tensors is denoted by $(\boldsymbol{AB})_{ij} = A_{ik}B_{kj}$ (similar to matrix multiplication). The second-order identity tensor is given by $\boldsymbol{I}_{ij} = \delta_{ij}$, where $\delta_{ij}$ is the Kronecker delta. The second-order zero tensor is denoted by $\mathbf{0}$.

Following the standard algebraic definitions, the inverse and transpose of a tensor $\boldsymbol{A}$ are denoted by $\boldsymbol{A}^{-1}$ and $\boldsymbol{A}^{\mathbf{T}}$ respectively. Using this notation, the symmetric and antisymmetric (also called skew-symmetric) parts of $\boldsymbol{A}$ can be calculated by $\mathbf{sym}\,(\boldsymbol{A}) = \frac{1}{2}\left(\boldsymbol{A} + \boldsymbol{A}^{\mathbf{T}}\right)$ and $\mathbf{skew}\,(\boldsymbol{A}) = \frac{1}{2}\left(\boldsymbol{A} - \boldsymbol{A}^{\mathbf{T}}\right)$ respectively. The trace and determinant of a tensor $\boldsymbol{A}$ are denoted by $\mathrm{tr}\,(\boldsymbol{A})$ and $\det(\boldsymbol{A})$ respectively. Using this notation, the deviator of the tensor $\boldsymbol{A}$ is determined as $\mathbf{dev}\,(\boldsymbol{A}) = \boldsymbol{A} - \frac{\mathrm{tr}(\boldsymbol{A})}{3}\boldsymbol{I}$. Finally, the Euclidean norm of the tensor is given by $\|\boldsymbol{A}\| = \sqrt{\boldsymbol{A} : \boldsymbol{A}}$.

## 2. Finite-strain elastoplasticity theory: Kinematics and conservation laws

### *2.1. Kinematics*

In this section, we summarize basic kinematic relationships required for the development of the proposed phenomenological model of ductile fracture. Consider a body with a placement $\Omega$ at time $t \in \mathbb{R}^+$ that can undergo plastic deformation. The motion of this body is described by a function $\boldsymbol{\varphi}$ that maps a material point $\boldsymbol{X}$ of the reference configuration $\Omega_0$ into a point $\boldsymbol{x} \in \Omega$ of the spatial (or current) configuration as follows

$$\boldsymbol{x} = \boldsymbol{\varphi}(\boldsymbol{X}, t)\,. \tag{1}$$

The difference between its current position and its reference position defines the unknown displacement vector

$$\boldsymbol{u}(\boldsymbol{X}, t) = \boldsymbol{x} - \boldsymbol{X} = \boldsymbol{\varphi}(\boldsymbol{X}, t) - \boldsymbol{X}\,. \tag{2}$$

The deformation gradient, which relates tangent vectors of reference and current configurations, is defined as follows

$$\boldsymbol{F} = \nabla_0 \boldsymbol{\varphi} = \frac{\partial \boldsymbol{\varphi}}{\partial \boldsymbol{X}} \,, \tag{3}$$

where $\nabla_0$ denotes the gradient operator with respect to the reference configuration.

We adopt a local multiplicative decomposition of the total deformation gradient [50], expressed by

$$\boldsymbol{F} = \boldsymbol{F}^e \boldsymbol{F}^p \,, \tag{4}$$

into elastic and plastic components ($\boldsymbol{F}^e$ and $\boldsymbol{F}^p$ respectively). This decomposition introduces three configurations as shown in Fig. 1 (namely, reference, intermediate, and spatial configurations) [51]. For the sake of clarity, a calligraphic font is used to denote quantities of the intermediate configuration. The deformation gradient maps a point $\boldsymbol{X}$ in the reference configuration to $\boldsymbol{\mathcal{X}}$ in the intermediate configuration by $\boldsymbol{F}^p$, and then to $\boldsymbol{x}$ in the spatial configuration $\Omega$ by $\boldsymbol{F}^e$. The intermediate configuration is local and incompatible in the sense that continuity of its neighborhoods is not guaranteed unless the deformation of the body is homogeneous [52].

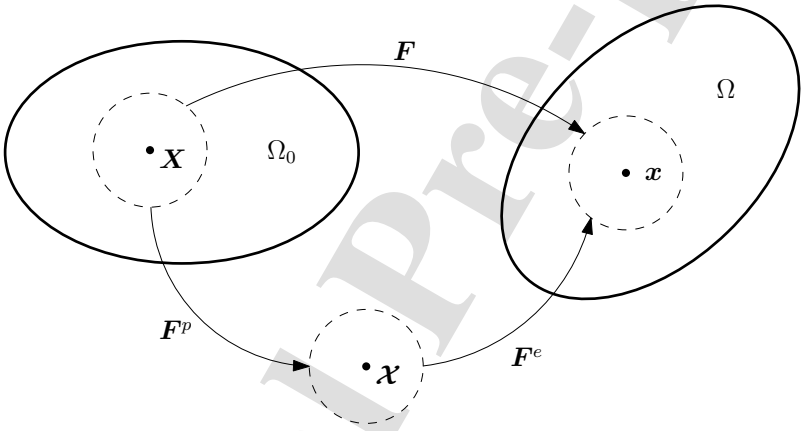


Figure 1: Multiplicative decomposition of the deformation gradient and definition of the intermediate configuration.

To formulate the necessary constitutive laws, we need to define kinematic and stress measures in these three configurations. In particular, the spatial velocity gradient is expressed by

$$\boldsymbol{l} = \dot{\boldsymbol{F}} \boldsymbol{F}^{-1} \,. \tag{5}$$

The (total) rate of deformation tensor $\boldsymbol{d}$ and the spin tensor $\widehat{\boldsymbol{w}}$ are defined as the symmetric and skew-symmetric parts of the spatial velocity gradient tensor as follows

$$\left.\begin{aligned} \boldsymbol{d}^\alpha &= \mathbf{sym}\,(\boldsymbol{l}^\alpha) \\ \widehat{\boldsymbol{w}}^\alpha &= \mathbf{skew}\,(\boldsymbol{l}^\alpha) \end{aligned}\right\} \,. \tag{6}$$

These definitions hold for the total quantities (superscript $\alpha$ is omitted), as well as for their elastic ($\alpha = e$) and plastic ($\alpha = p$) parts; see Appendix A.1 for details.

Assuming that $\widehat{\boldsymbol{w}}^p = \boldsymbol{0}$ and isochoric plastic response, the $J_2$ flow rule is expressed in terms of the plastic rate of deformation tensor as follows

$$\boldsymbol{d}^p = \dot{\bar{\varepsilon}}_p \, \boldsymbol{n}^p \,, \tag{7}$$

where $\bar{\varepsilon}_p$ is the equivalent viscoplastic strain and $\boldsymbol{n}^p$ denotes the direction of viscoplastic flow, represented as a second-order tensor. Further elaboration on the imposed constraints in $J_2$ flow theory is provided in Appendix A.2.

### *2.2. Conservation laws*

In this section, we briefly present the differential equations that describe the conservation laws of the proposed thermomechanical system. Interested readers are referred to [53] for more details on the derivation.

- Balance of linear momentum:

$$\nabla_0 \cdot \boldsymbol{P} + \rho_0 \bar{\boldsymbol{B}} = \rho_0 \ddot{\boldsymbol{u}} \,, \tag{8}$$

  where $\boldsymbol{P}$ denotes the first Piola-Kirchhoff stress (see Appendix A.3 for details relating to different stress measures), $\rho_0$ is the density in reference configuration, $\rho_0 \bar{\boldsymbol{B}}$ expresses the volume force, and $\nabla_0 \cdot$ denotes the divergence operator with respect to the reference configuration.

- Balance of microforces: To derive the phase-field equation, we assume the existence of micro-forces. Specifically, $f_e$ and $f_i \in \mathbb{R}$ denote the external and internal micro-forces respectively, while $\boldsymbol{\Xi}$ is a micro-force traction vector [42, 54].

$$\nabla_0 \cdot \boldsymbol{\Xi} + f_e - f_i = 0 \,. \tag{9}$$

- First law of thermodynamics: We also express the balance law which postulates the conservation of energy in thermomechanical processes. Let $e$ denote the internal energy (per unit mass) and consider the mechanisms that can change the aforementioned energy (elasto-plastic deformation and fracture). We assume that $\nabla_0 \dot{d}$ and $\dot{d}$ are the power conjugate quantities to micro-force traction vector and micro-forces respectively. Hence, the balance law of conservation of energy reads [55]

$$\rho_0 \dot{e} = \boldsymbol{P} : \dot{\boldsymbol{F}} + \boldsymbol{\Xi} \cdot \nabla_0 \dot{d} + f_i \dot{d} - \nabla_0 \cdot \boldsymbol{Q} \,, \tag{10}$$

  where $\boldsymbol{Q}$ is the heat-flux vector at the reference configuration.

## 3. Formulation of constitutive relations: Minimum principle and Clausius–Duhem inequality

In this section, we derive a visco-plastic flow rule using a variational formulation of thermomechanical constitutive relations and the second law of thermodynamics for generalized standard materials (GSMs). After defining the state variables and energy-related functions for GSMs, we express the minimum principle, similar to [12, 20]. Finally, we employ the second law of thermodynanics (in the form of the Clausius-Duhem inequality) to arrive at the expression of the internal power dissipation density which plays a critical role in the minimization problem. By analytically applying the minimum principle, we determine the evolution equations of the internal variables expressed as a standard associative plastic flow rule in this work.

### 3.1. Variational formulation: A minimum principle in generalized standard materials

For the sake of compact notation, we group the state variables as follows: (i) $\mathfrak{M} = \{\boldsymbol{\mathcal{C}}^e, d, \nabla_0 d\}$ characterizes the mechanical state ($\boldsymbol{\mathcal{C}}^e$ denotes the elastic right Cauchy-Green tensor), (ii) $\mathfrak{Z} = \{\bar{\varepsilon}_p\}$ are internal-state variables which describe dissipative phenomena, and (iii) $\mathfrak{E} = \{e, \eta, T\}$ are thermodynamic variables, including the specific entropy $\eta$ and the absolute temperature $T$.

Adopting the concept of GSMs [11, 14], we postulate the existence of a Helmholtz free energy (per unit mass) $\psi = \psi(\mathfrak{M}, T, \mathfrak{Z})$ and a dissipation pseudo-potential (per unit mass) $\phi = \phi(\dot{\mathfrak{M}}, \dot{\mathfrak{Z}}; \mathfrak{M}, T, \mathfrak{Z})$. Note that the dissipation pseudo-potential does not depend on the temperature rate $\dot{T}$. The Helmholtz free energy is defined as follows

$$\psi = e - T\eta\,, \tag{11}$$

and the definition of specific entropy reads as follows

$$\eta = -\frac{\partial \psi}{\partial T}\,. \tag{12}$$

Furthermore, we assume that the state variables are known and fixed while $\dot{\mathfrak{M}}$ and $\dot{\mathfrak{E}}$ are calculated from the balance laws in conjunction with the definitions in Eqs. (11) and (12) and the second law of thermodynamics. To find the evolution of the internal variables $\mathfrak{Z}$, the following minimum principle is postulated [12, 20]

$$\inf_{\boldsymbol{n}^p, \dot{\mathfrak{Z}}} \mathfrak{D}(\dot{\mathfrak{S}}; \mathfrak{S})\,, \tag{13}$$

where the state variables are expressed by $\mathfrak{S} = \{\mathfrak{M}, \mathfrak{E}, \mathfrak{Z}\}$ and the functional $\mathfrak{D}$ is introduced as follows

$$\mathfrak{D} = \rho_0 \dot{e} - \rho_0 T \dot{\eta} + \rho_0 \phi\,. \tag{14}$$

This functional is the summation of three components, each representing a power per unit volume for both reversible and irreversible processes. By solving the optimization problem, we can determine the equivalent viscoplastic strain $\bar{\varepsilon}_p$ and flow direction $\boldsymbol{n}^p$. Assuming that the thermomechanical system under consideration is governed by a single type of temperature, the absolute temperature $T$ (i.e., "equilibrium" and absolute temperatures are approximately equal as defined in [18]), we can substitute Eq. (11) into Eq. (14) and arrive at the variational formulation expressed by the functional as follows

$$\mathfrak{D} = \rho_0 \dot{\psi} + \rho_0 \phi + \rho_0 \dot{T} \eta\,. \tag{15}$$

In the following sections, we will derive the evolution equations of the internal variables by minimizing the aforementioned thermodynamic quantity.

### 3.2. Second law of thermodynamics: Coleman-Noll procedure and plastic dissipation

In this section, we formulate constitutive relations that adhere to the second law of thermodynamics, which asserts that entropy production is always greater than zero. The Clausius-Duhem form of this law can be recast into the following inequality

$$\mathbb{D} = \mathbb{D}^{int} + \mathbb{D}^{con} \geq 0\,, \tag{16}$$

where the dissipation arising from heat conduction $\mathbb{D}^{con}$ and internal power dissipation density $\mathbb{D}^{int}$ are defined by

$$\left.\begin{aligned}\mathbb{D}^{con} &= -\frac{1}{T}\boldsymbol{Q}\cdot\nabla_0 T\\ \mathbb{D}^{int} &= \rho_0 T\dot{\eta}+\nabla_0\cdot\boldsymbol{Q}\end{aligned}\right\}. \tag{17}$$

Following the Coleman-Noll procedure presented in Appendix B, we arrive at the relations

$$\left.\begin{aligned}\boldsymbol{\tau} &= 2\rho_0\boldsymbol{F}^e\frac{\partial\psi}{\partial\boldsymbol{\mathcal{C}}^e}\boldsymbol{F}^{e\mathbf{T}}\\ \boldsymbol{\Xi} &= \rho_0\frac{\partial\psi}{\partial\nabla_0 d}\\ f_i &= \rho_0\frac{\partial\psi}{\partial d}\end{aligned}\right\}, \tag{18}$$

and the inequality related to the internal power dissipation density

$$\mathbb{D}^{int}=\mathbb{D}^{p}-Y_s^p\dot{\bar{\varepsilon}}_p=\left(\boldsymbol{\tau}:\boldsymbol{n}^p-Y_s^p\right)\dot{\bar{\varepsilon}}_p\geq 0\,, \tag{19}$$

where the term $\mathbb{D}^p$ denotes the plastic dissipation, and the generalized "thermodynamic forces" associated with plastic deformation, $\boldsymbol{P}^p$ (power conjugate to $\boldsymbol{F}^p$) and $Y_s^p$ (power conjugate to $\dot{\bar{\varepsilon}}_p$), are defined as follows

$$\left.\begin{aligned}\boldsymbol{P}^p &= \rho_0\frac{\partial\psi}{\partial\boldsymbol{F}^p}\\ Y_s^p &= \rho_0\frac{\partial\psi}{\partial\bar{\varepsilon}_p}\end{aligned}\right\}. \tag{20}$$

### *3.3. Derivation of the flow rule from the minimum principle*

In this section, we assume a simple form of internal power dissipation density and show its compatibility with the proposed variational formulation. To derive the viscoplastic flow rule, we apply the minimum principle introduced in Eq. (13) while imposing a constraint on a yield function $\widehat{\Phi}_y\leq 0$.

First, we assume that the form of internal power dissipation density is given, in agreement with Eq. (19), by

$$\mathbb{D}^{int}=Y_v^p\dot{\bar{\varepsilon}}_p\geq 0 \tag{21}$$

where the generalized dissipative (viscous) thermodynamic force $Y_v^p$ can be found by using the minimum principle. Specifically, the *constrained* optimization problem reads as follows

$$\inf_{\boldsymbol{n}^p,\dot{\bar{\varepsilon}}_p}\ \mathfrak{D}\,, \tag{22}$$

subject to the constraint on the von Mises yield function in $J_2$ plasticity theory as follows

$$\widehat{\Phi}_y=s_v-Y_s^p-Y_v^p\leq 0\,, \tag{23}$$

where $s_v$ denotes the von Mises stress.

By minimizing the functional $\mathfrak{D}$ in Eq. (15) with respect to $\dot{\bar{\varepsilon}}_p$, the generalized dissipative force $Y_v^p$ is expressed in terms of the dissipation pseudo-potential as follows [12]

$$Y_v^p=\rho_0\frac{\partial\phi}{\partial\dot{\bar{\varepsilon}}_p}. \tag{24}$$

By minimizing the functional $\mathfrak{D}$ in Eq. (15) with respect to $\boldsymbol{n}^p$ and imposing the constraints outlined in Appendix A.2, we determine the viscoplastic flow direction

$$\boldsymbol{n}^p = \sqrt{\frac{3}{2}}\frac{\boldsymbol{s}}{\|\boldsymbol{s}\|} = \frac{3}{2}\frac{\boldsymbol{s}}{s_v}\,, \tag{25}$$

where $\boldsymbol{s}$ denotes the deviator of the Kirchhoff stress tensor $\boldsymbol{\tau}$.

The Karush-Kuhn-Tucker (KKT) conditions expressed as plastic loading/unloading conditions read

$$\dot{\bar{\varepsilon}}_p \geq 0 \quad \text{and} \quad \widehat{\Phi}_y \leq 0 \quad \text{and} \quad \widehat{\Phi}_y \dot{\bar{\varepsilon}}_p = 0\,. \tag{26}$$

The viscoplastic flow rule (according to Eq. (7)) is derived as follows

$$\boldsymbol{d}^p = \frac{3}{2}\dot{\bar{\varepsilon}}_p \frac{\boldsymbol{s}}{s_v} \tag{27}$$

The last equation describes an associative plastic flow rule which is similar to the one presented in [10, 56]. Finally, substituting the viscoplastic flow direction (Eq. (25)) into Eq. (19) and combining the result with Eq. (21), we arrive at the inequality of internal power dissipation density

$$\mathbb{D}^{int} = \left[\sqrt{\frac{3}{2}}\|\boldsymbol{s}\| - Y_s^p\right]\dot{\bar{\varepsilon}}_p = Y_v^p \dot{\bar{\varepsilon}}_p \geq 0. \tag{28}$$

It is noteworthy that the form of internal power dissipation density is compatible with the KKT conditions.

## 4. Ductile fracture model: Energy specifications and governing equations

### *4.1. Form of free energy and dissipation pseudo-potential*

The total free energy is additively decomposed into elastic, fracture, plastic and thermal components as follows

$$\psi(\mathfrak{M}, T, \mathfrak{Z}) = \psi^e(\boldsymbol{\mathcal{C}}^e, d) + \psi^f(d, \nabla_0 d) + \psi^p(d, T, \bar{\varepsilon}_p) + \psi^\theta(T)\,, \tag{29}$$

and the dissipation pseudo-potential has only a viscoplastic component

$$\phi = \phi(\dot{\mathfrak{M}}, \dot{\mathfrak{Z}}; \mathfrak{M}, T, \mathfrak{Z}) = \phi^p(\dot{\bar{\varepsilon}}_p; d, T, \bar{\varepsilon}_p)\,. \tag{30}$$

In the phase-field fracture method, the fracture component of the Helmholtz free energy is a function of phase field and its gradient [57] as follows

$$\rho_0 \psi^f = \frac{G_c}{2\ell_0}\left(d^2 + \ell_0^2\,|\nabla_0 d|^2\right)\,, \tag{31}$$

where $G_c$ is the critical energy release rate, and $\ell_0$ is a regularization length-scale.

We assume that all the remaining components depend on phase field $d$, except the thermal free energy, which is given by

$$\rho_0 \psi^\theta = \rho_0 C_v\left[(T - T_0) - T\ln\frac{T}{T_0}\right]\,, \tag{32}$$

where $T_0$ is a reference temperature, and $C_v$ denotes the specific heat capacity.

**Remark 4.1.** *Notice that viscoelastic effects are ignored in this work, and we assume that fracture does not cause any heat generation.*

*4.1.1. Hyperelastic model*

In this model, the elastic strain energy is degraded due to damage following the law

$$\rho_0 \psi^e = g^e(d) W^+(\boldsymbol{\mathcal{C}}^e) + W^-(\boldsymbol{\mathcal{C}}^e)\,, \tag{33}$$

where $W^+$ and $W^-$ are the "tensile" and "compressive" contributions respectively. In the numerical simulations of this work, the elastic degradation function is described by $g^e(d) = (1-d)^2 + g_1^e$, where $g_1^e = 10^{-9}$ is used as a residual value to prevent numerical instabilities after crack formation ($d = 1$). Notice that the degradation function applies only to the tensile part while the compressive part is not affected.

The elastic response is governed by a constitutive model in which strain energy is decomposed into volumetric and deviatoric components. Specifically, we follow the strain energy decomposition presented in [51, 58]. To this end, we introduce

$$\bar{\boldsymbol{\mathcal{C}}}^e = J^{e-\frac{2}{3}} \boldsymbol{\mathcal{C}}^e\,, \tag{34}$$

and the volumetric and deviatoric components are defined as follows (p. 307 in [51])

$$\left.\begin{aligned} U(J^e) &= \frac{1}{2}\kappa \left[\frac{1}{2}\left(J^{e2}-1\right) - \ln J^e\right] \\ \bar{W}(\bar{\boldsymbol{\mathcal{C}}}^e) &= \frac{1}{2}\mu \left[\mathrm{tr}\left(\bar{\boldsymbol{\mathcal{C}}}^e\right) - 3\right] \end{aligned}\right\}. \tag{35}$$

where $\kappa$ and $\mu$ are the bulk and the shear modulus respectively.

With this energy decomposition at hand, the damaged elastic strain energy is rewritten as

$$\rho_0 \psi^e = g^e(d) W^+(J^e, \bar{\boldsymbol{\mathcal{C}}}^e) + W^-(J^e) \tag{36}$$

where the tensile part is given by

$$W^+ = \begin{cases} U(J^e) + \bar{W}(\bar{\boldsymbol{\mathcal{C}}}^e), & J^e \geq 1 \\ \bar{W}(\bar{\boldsymbol{\mathcal{C}}}^e), & 0 < J^e < 1 \end{cases} \tag{37}$$

whereas the compressive part by

$$W^- = \begin{cases} 0, & J^e \geq 1 \\ U(J^e), & 0 < J^e < 1 \end{cases} \tag{38}$$

*4.1.2. A class of thermo-viscoplasticity models*

Inspired by the work of Ranc and Chrysochoos [59], we present a framework for the representation of a broad class of rheological (evolution) equations. The goal of this section is to consistently couple thermo-viscoplasticity models (such as the Johnson-Cook model [6]) with the phase-field fracture approach in the context of the generalized standard materials.

The *undamaged* stored energy density due to plastic work, denoted by $W^p$, defines a plastic stress $\sigma_s$, while the *undamaged* dissipation pseudo-potential (per unit volume), denoted by $R^p$, defines a viscous stress $\sigma_v$ as follows

$$\left.\begin{aligned} \sigma_s &= \frac{\partial W^p}{\partial \bar{\varepsilon}_p} \\ \sigma_v &= \frac{\partial R^p}{\partial \dot{\bar{\varepsilon}}_p} \end{aligned}\right\}. \tag{39}$$

In the proposed model, the plastic component of Helmholtz free energy is degraded as follows

$$\rho_0 \psi^p = g^p(d) W^p(\bar{\varepsilon}_p, T)\,, \tag{40}$$

while the dissipation pseudo-potential is given by

$$\rho_0 \phi^p = g^p(d) R^p(\dot{\bar{\varepsilon}}_p; \bar{\varepsilon}_p, T)\,, \tag{41}$$

where the same plastic degradation function $g^p(d)$ is adopted. Using Eqs. (23) and (24), the evolution of the internal variable $\bar{\varepsilon}_p$ (which is described by the KKT conditions given in Eq. (26) when $\dot{\bar{\varepsilon}}_p \neq 0$) reads

$$\widehat{\Phi}_y = 0 \Rightarrow s_v = \rho_0 \frac{\partial \psi}{\partial \bar{\varepsilon}_p} + \rho_0 \frac{\partial \phi}{\partial \dot{\bar{\varepsilon}}_p}\,. \tag{42}$$

Substituting Eqs. (40) and (41) into Eq. (42), the evolution equation of $\bar{\varepsilon}_p$ can be simplified as follows

$$s_v = g^p(d) \left( \frac{\partial W^p}{\partial \bar{\varepsilon}_p} + \frac{\partial R^p}{\partial \dot{\bar{\varepsilon}}_p} \right) = g^p(d) \left( \sigma_s + \sigma_v \right)\,. \tag{43}$$

In the next parts of this section, we construct the *undamaged* stored plastic free energy and dissipation pseudo-potential such that an additive decomposition of stresses holds as follows

$$\sigma_s(\bar{\varepsilon}_p, T) + \sigma_v(\bar{\varepsilon}_p, \dot{\bar{\varepsilon}}_p, T) = \sigma_y(\bar{\varepsilon}_p, \dot{\bar{\varepsilon}}_p, T)\,, \tag{44}$$

where $\sigma_y$ denotes a temperature-dependent viscoplastic flow stress for a broad class of material models. In this way, the dependence of von Mises stress on the phase field and yield stress (according to Eq. (43)) reads as follows

$$s_v = g^p(d) \sigma_y(\bar{\varepsilon}_p, \dot{\bar{\varepsilon}}_p, T)\,, \tag{45}$$

where the right-hand side of the above equation describes the *damaged* yield stress.

*A novel plastic degradation function.* When a material point is fully damaged ($d = 1$), the evolution equation for the equivalent plastic strain $\bar{\varepsilon}_p$, given in Eq. (45), loses its physical meaning because the material can no longer accumulate plastic deformation. This results in numerical instabilities, manifested as divergence in our algorithm and excessive increases in the values of $\bar{\varepsilon}_p$.

In the literature, one strategy for stabilizing the numerical scheme involves incorporating a re-scaling factor into the gradient term of the plastic energy threshold in the phase-field equation, as suggested by [60]. An alternative method is a modified degradation function proposed by [61], where its polynomial form is normalized by the accumulative plastic strain.

In this work, we propose a novel plastic degradation function to account for the gradual contribution of the stored plastic work to fracture, and the non-vanishing values of the damage-dependent yield stress. To this end, we construct a cubic degradation function that satisfies the following conditions

$$\left.\begin{aligned} & g^p(0) = 1 \\ & g^p(1) = \mathrm{g_f} \\ & \left.\frac{\partial g^p}{\partial d}\right|_{d=0} = \mathrm{s_0} \\ & \left.\frac{\partial g^p}{\partial d}\right|_{d=1} = 0 \end{aligned}\right\}\,, \tag{46}$$

where $s_0$ controls the initial slope when the material is intact, and $g_f$ represents the residual value of the plastic degradation function when the material is fully damaged. It is noteworthy that even though $g^p(1) \neq 0$, the crack driving force associated with its first derivative vanishes at $d = 1$. Hence, the role of $s_0$ is analogous to the plastic energy threshold introduced by [35] in delaying the damage evolution after the accumulation of plastic energy. Its value should be negative and close to zero (e.g., $s_0 = -0.01$ unless otherwise stated in the numerical results of this manuscript). By imposing the above conditions, we arrive at the proposed plastic degradation function

$$g^p(d) = (2 - 2g_f + s_0)d^3 + (-3 + 3g_f - 2s_0)d^2 + s_0 d + 1\,. \tag{47}$$

The impact of $g_f$ on our proposed formulation is explored in the section on numerical examples.

*Generalized representation of flow stress.* In this work, we study a class of thermo-viscoplasticity models in which the flow stress depends on plastic strain, strain-rate, and temperature. We assume a multiplicative decomposition of the flow stress as follows

$$\sigma_y(\bar{\varepsilon}_p, \dot{\bar{\varepsilon}}_p, T) = f_p(\bar{\varepsilon}_p; \mathfrak{P}_p) f_v(\dot{\bar{\varepsilon}}_p, T; \mathfrak{P}_v) f_\theta(T; \mathfrak{P}_\theta)\,, \tag{48}$$

where $\mathfrak{P}_p$, $\mathfrak{P}_v$ and $\mathfrak{P}_\theta$ denote material parameters corresponding to the functions $f_p$, $f_v$, and $f_\theta$ respectively. Notice that $f_v$ depends on both $\dot{\bar{\varepsilon}}_p$ and $T$, while the other functions have only one argument.

If $f_v$ is independent of $T$ (i.e. $\frac{\partial f_v}{\partial T} = 0$), the multiplicative decomposition is unique (up to constant multipliers). For example, the flow stress in the Johnson-Cook model [6] is a function of $\bar{\varepsilon}_p, \dot{\bar{\varepsilon}}_p$, and $T$ as follows

$$\sigma_y(\bar{\varepsilon}_p, \dot{\bar{\varepsilon}}_p, T) = \left(A + B\bar{\varepsilon}_p^m\right)\left(1 + C\ln\dot{\bar{\varepsilon}}_*\right)(1 - \theta_*^q)\,, \tag{49}$$

where $A, B, C, m$, and $q$ are material parameters and the normalized strain-rate is defined by $\dot{\bar{\varepsilon}}_* = \frac{\dot{\bar{\varepsilon}}_p}{\dot{\bar{\varepsilon}}_0}$ and the homologous temperature is given by $\theta_* = \frac{T - T_t}{T_m - T_t}$, where $\dot{\bar{\varepsilon}}_0$ is a reference strain-rate and $T_t$ and $T_m$ are transition and melting temperatures respectively. Hence, the factors of the flow stress read

$$\left.\begin{aligned} &f_p(\bar{\varepsilon}_p; \mathfrak{P}_p) = A + B\bar{\varepsilon}_p^m \text{ where } \mathfrak{P}_p = \{A, B, m\} \\ &f_v(\dot{\bar{\varepsilon}}_p, T; \mathfrak{P}_v) = 1 + C\ln\dot{\bar{\varepsilon}}_* \text{ where } \mathfrak{P}_v = \{C, \dot{\bar{\varepsilon}}_0\} \\ &f_\theta(T; \mathfrak{P}_\theta) = 1 - \theta_*^q \text{ where } \mathfrak{P}_\theta = \{T_t, T_m, q\} \end{aligned}\right\}\,. \tag{50}$$

Inspired by the work of Simo and Hughes [51], we propose an extended Johnson-Cook (XJC) plasticity model with a nonlinear hardening law. The proposed flow stress, which incorporates two additional material parameters (namely, the ultimate stress $A^u$ and the saturation parameter $\delta$), is given by the function

$$\sigma_y(\bar{\varepsilon}_p, \dot{\bar{\varepsilon}}_p, T) = \left(A^u + B\bar{\varepsilon}_p^m - (A^u - A)\exp\left(-\delta\bar{\varepsilon}_p\right)\right)\left(1 + C\ln\dot{\bar{\varepsilon}}_*\right)(1 - \theta_*^q)\,. \tag{51}$$

The factors of flow stress are expressed as

$$\left.\begin{aligned} &f_p(\bar{\varepsilon}_p; \mathfrak{P}_p) = A^u + B\bar{\varepsilon}_p^m - (A^u - A)\exp\left(-\delta\bar{\varepsilon}_p\right) \text{ where } \mathfrak{P}_p = \{A, A^u, B, m, \delta\} \\ &f_v(\dot{\bar{\varepsilon}}_p, T; \mathfrak{P}_v) = 1 + C\ln\dot{\bar{\varepsilon}}_* \text{ where } \mathfrak{P}_v = \{C, \dot{\bar{\varepsilon}}_0\} \\ &f_\theta(T; \mathfrak{P}_\theta) = 1 - \theta_*^q \text{ where } \mathfrak{P}_\theta = \{T_t, T_m, q\} \end{aligned}\right\}\,. \tag{52}$$

However, these types of decomposition are not always unique (e.g., in the case of a function $f_v$ that explicitly depends on $T$). For instance, the flow stress in a modified Zerilli-Armstrong model [62] is a function of $\bar{\varepsilon}_p, \dot{\bar{\varepsilon}}_p$, and $T$ as follows

$$\sigma_y(\bar{\varepsilon}_p, \dot{\bar{\varepsilon}}_p, T) = \left(A + B\bar{\varepsilon}_p^m\right) \exp\left(-C_3 T + C_4 T \ln \dot{\bar{\varepsilon}}_*\right), \tag{53}$$

and $f_v(\dot{\bar{\varepsilon}}_p, T; \mathfrak{P}_v)$ can be chosen as $\exp\left(-C_3 T + C_4 T \ln \dot{\bar{\varepsilon}}_*\right)$ or $\exp\left(C_4 T \ln \dot{\bar{\varepsilon}}_*\right)$ (and many other functions). To address this issue, we select the function that satisfies the following condition

$$f_v(\dot{\bar{\varepsilon}}_p, T; \mathfrak{P}_v) = \frac{\sigma_y(\bar{\varepsilon}_p, \dot{\bar{\varepsilon}}_p, T)}{\sigma_y(\bar{\varepsilon}_p, \dot{\bar{\varepsilon}}_0, T)} = \exp\left(C_4 T \ln \dot{\bar{\varepsilon}}_*\right). \tag{54}$$

Hence, the factors of the flow stress read

$$\left.\begin{aligned} f_p(\bar{\varepsilon}_p; \mathfrak{P}_p) &= A + B\bar{\varepsilon}_p^m \text{ where } \mathfrak{P}_p = \{A, B, m\} \\ f_v(\dot{\bar{\varepsilon}}_p, T; \mathfrak{P}_v) &= \exp\left(C_4 T \ln \dot{\bar{\varepsilon}}_*\right) \text{ where } \mathfrak{P}_v = \{C_4, \dot{\bar{\varepsilon}}_0\} \\ f_\theta(T; \mathfrak{P}_\theta) &= \exp\left(-C_3 T\right) \text{ where } \mathfrak{P}_\theta = \{C_3\} \end{aligned}\right\}. \tag{55}$$

**Remark 4.2.** *Eq. (54) can be seen as a normalization condition. This type of condition is also used in the Johnson-Cook (JC) model to find the unique factors and calculate the unknown constant multipliers.*

Furthermore, we assume that the function $f_p$ is additively decomposed into two parts, namely, stored and dissipative components as follows

$$f_p(\bar{\varepsilon}_p; \mathfrak{P}_p) = f_p(\bar{\varepsilon}_p; \mathfrak{P}_{p_s}) + f_p(\bar{\varepsilon}_p; \mathfrak{P}_{p_d}), \tag{56}$$

where $\mathfrak{P}_{p_s}$ and $\mathfrak{P}_{p_d}$ are material parameters that characterize the stored and dissipative components respectively. In this work, we adopt the power law (as shown in Eqs. (50) and (55))

$$\left.\begin{aligned} f_p(\bar{\varepsilon}_p; \mathfrak{P}_p) &= A + B\bar{\varepsilon}_p^m \text{ where } \mathfrak{P}_p = \{A, B, m\} \\ f_p(\bar{\varepsilon}_p; \mathfrak{P}_{p_s}) &= A_s + B_s\bar{\varepsilon}_p^{m_s} \text{ where } \mathfrak{P}_{p_s} = \{A_s, B_s, m_s\} \\ f_p(\bar{\varepsilon}_p; \mathfrak{P}_{p_d}) &= A_d + B_d\bar{\varepsilon}_p^{m_d} \text{ where } \mathfrak{P}_{p_d} = \{A_d, B_d, m_d\} \end{aligned}\right\}, \tag{57}$$

where $A = A_s + A_d$, $B = B_s + B_d$, and $m = m_s = m_d$. We introduce partial Taylor-Quinney (TQ) coefficients, $\chi_A$ and $\chi_B$, associated with parameters $A$ and $B$ respectively, to control the fraction of the plastic work that will be converted into heat (the latter is related to dissipative components) as shown below

$$\left.\begin{aligned} A_d = \chi_A A \Rightarrow A_s = (1 - \chi_A)A \\ B_d = \chi_B B \Rightarrow B_s = (1 - \chi_B)B \end{aligned}\right\}. \tag{58}$$

Given the generalized representation of flow stress as expressed in Eq. (48), the undamaged stored viscoplastic free energy density and dissipation pseudo-potential can be expressed as follows

$$\left.\begin{aligned} W^p(\bar{\varepsilon}_p, T) &= F_p(\bar{\varepsilon}_p; \mathfrak{P}_{p_s}) f_\theta(T; \mathfrak{P}_\theta) \\ R^p(\dot{\bar{\varepsilon}}_p, \bar{\varepsilon}_p, T) &= \left[f_p(\bar{\varepsilon}_p; \mathfrak{P}_{p_d})\dot{\bar{\varepsilon}}_p + f_p(\bar{\varepsilon}_p; \mathfrak{P}_p)\hat{F}_v(\dot{\bar{\varepsilon}}_p, T; \mathfrak{P}_v)\right] f_\theta(T; \mathfrak{P}_\theta) \end{aligned}\right\}, \tag{59}$$

where

$$\left.\begin{aligned} F_p(\bar{\varepsilon}_p;\mathfrak{P}_{p_s}) &= \int_0^{\bar{\varepsilon}_p} f_p(\hat{p};\mathfrak{P}_{p_s})\,\mathrm{d}\hat{p} \\ \hat{F}_v(\dot{\bar{\varepsilon}}_p,T;\mathfrak{P}_v) &= F_v(\dot{\bar{\varepsilon}}_p,T;\mathfrak{P}_v) - \left(\dot{\bar{\varepsilon}}_p - \dot{\bar{\varepsilon}}_0\right) \\ F_v(\dot{\bar{\varepsilon}}_p,T;\mathfrak{P}_v) &= \int_{\dot{\bar{\varepsilon}}_0}^{\dot{\bar{\varepsilon}}_p} f_v(\hat{r},T;\mathfrak{P}_v)\,\mathrm{d}\hat{r} \end{aligned}\right\}. \tag{60}$$

*Johnson-Cook model.* As a simple case of this framework, the undamaged stored energy density due to plastic work and dissipation pseudo-potential (per unit volume) are derived from Eq. (59) based on the analytical expression of the Johnson-Cook model [6] (cf. functions in [20]):

$$\left.\begin{aligned} W^p(\bar{\varepsilon}_p,T) &= \left(A_s\bar{\varepsilon}_p + \frac{B_s}{m+1}\bar{\varepsilon}_p^{m+1}\right)(1-\theta_*^q) \\ R^p(\dot{\bar{\varepsilon}}_p,\bar{\varepsilon}_p,T) &= \left[\left(A_d + B_d\bar{\varepsilon}_p^m\right)\dot{\bar{\varepsilon}}_p + \left(A + B\bar{\varepsilon}_p^m\right)C\dot{\bar{\varepsilon}}_0\left(\dot{\bar{\varepsilon}}_*\ln\dot{\bar{\varepsilon}}_* - \dot{\bar{\varepsilon}}_* + 1\right)\right](1-\theta_*^q) \end{aligned}\right\}. \tag{61}$$

*Extended Johnson-Cook model.* Applying the same framework, the energy and dissipation functions for our proposed modification of the JC model with a nonlinear hardening law read:

$$\left.\begin{aligned} W^p(\bar{\varepsilon}_p,T) &= \left(A_s^u\bar{\varepsilon}_p + \frac{B_s}{m+1}\bar{\varepsilon}_p^{m+1} + (A_s^u - A_s)\exp\left(-\delta\bar{\varepsilon}_p\right)/\delta\right)(1-\theta_*^q) \\ R^p(\dot{\bar{\varepsilon}}_p,\bar{\varepsilon}_p,T) &= \Big[\left(A_d^u + B_d\bar{\varepsilon}_p^m - (A_d^u - A_d)\exp\left(-\delta\bar{\varepsilon}_p\right)\right)\dot{\bar{\varepsilon}}_p \\ &\quad + \left(A^u + B\bar{\varepsilon}_p^m - (A^u - A)\exp\left(-\delta\bar{\varepsilon}_p\right)\right)C\dot{\bar{\varepsilon}}_0\left(\dot{\bar{\varepsilon}}_*\ln\dot{\bar{\varepsilon}}_* - \dot{\bar{\varepsilon}}_* + 1\right)\Big](1-\theta_*^q) \end{aligned}\right\} \tag{62}$$

where $A^u = A_d^u + A_s^u$.

*Modified Zerilli-Armstrong model.* To show the versatility of the proposed framework, the following functions are derived from Eq. (59) for the modified Zerilli-Armstrong model [62]:

$$\left.\begin{aligned} W^p(\bar{\varepsilon}_p,T) &= \left(A_s\bar{\varepsilon}_p + \frac{B_s}{m+1}\bar{\varepsilon}_p^{m+1}\right)\exp\left(-C_3T\right) \\ R^p(\dot{\bar{\varepsilon}}_p,\bar{\varepsilon}_p,T) &= \left\{\left(A_d + B_d\bar{\varepsilon}_p^m\right)\dot{\bar{\varepsilon}}_p + \left(A + B\bar{\varepsilon}_p^m\right)\frac{\dot{\bar{\varepsilon}}_0}{C_4T+1}\left[\left(\dot{\bar{\varepsilon}}_*\right)^{C_4T+1} - (C_4T+1)\,\dot{\bar{\varepsilon}}_* + C_4T\right]\right\}\exp\left(-C_3T\right) \end{aligned}\right\}. \tag{63}$$

### *4.2. Derivation of governing equations*

#### *4.2.1. Momentum equation*

The balance of linear momentum in the reference configuration reads

$$\nabla_0\cdot(\boldsymbol{F}\boldsymbol{S}) + \rho_0\bar{\boldsymbol{B}} = \rho_0\ddot{\boldsymbol{u}}\,, \tag{64}$$

where the second Piola-Kirchhoff stress (at the reference configuration) is given by a pullback operation of Eq. $(18)_1$

$$\boldsymbol{S} = 2g^e(d)\boldsymbol{F}^{p\text{-}\mathbf{1}}\left(\frac{\partial W^+}{\partial\boldsymbol{\mathcal{C}}^e}\right)\boldsymbol{F}^{p\text{-}\mathbf{T}} + 2\boldsymbol{F}^{p\text{-}\mathbf{1}}\left(\frac{\partial W^-}{\partial\boldsymbol{\mathcal{C}}^e}\right)\boldsymbol{F}^{p\text{-}\mathbf{T}}\,. \tag{65}$$

Dirichlet boundary conditions for displacement and velocity fields are prescribed as reported in the numerical examples.

*4.2.2. Phase-field equation*

Herein, we derive the phase-field equation from the balance of microforces given in Eq. (9). First, we substitute Eq. (18) into the microforce balance equation leading to

$$\rho_0 \nabla_0 \cdot \left( \frac{\partial \psi}{\partial \nabla_0 d} \right) + f_e - \rho_0 \frac{\partial \psi}{\partial d} = 0 \,. \tag{66}$$

Assuming $f_e = 0$ and adopting the free energy decomposition as shown in Eq. (29), the aforementioned equation is simplified as follows

$$\nabla_0 \cdot \left( \frac{\partial \psi^f}{\partial \nabla_0 d} \right) = \frac{\partial \psi^e}{\partial d} + \frac{\partial \psi^f}{\partial d} + \frac{\partial \psi^p}{\partial d} \,. \tag{67}$$

Using the specific forms of free energies as introduced in Section 4, we derive the phase-field equation

$$-G_c \ell_0 \Delta_0 d + \frac{G_c}{\ell_0} d + \frac{\partial g^e}{\partial d} W^+ + \frac{\partial g^p}{\partial d} W^p = 0 \,, \tag{68}$$

where $\Delta_0$ denotes the Laplace operator in the reference configuration. Crack irreversibility is enforced by introducing two history variables: $\mathcal{H}^+ = \max_t(W^+)$ and $\mathcal{H}^p = \max_t(W^p)$. Finally, Neumann boundary conditions are imposed and expressed as $\nabla_0 d \cdot \boldsymbol{n} = 0$, where $\boldsymbol{n}$ denotes the outward normal vector at the boundary.

*4.2.3. Heat equation*

Combining Eqs. (17) and (21), the heat equation is expressed as follows

$$\rho_0 T \dot{\eta} = -\nabla_0 \cdot \boldsymbol{Q} + Y_v^p \dot{\bar{\varepsilon}}_p \,, \tag{69}$$

where Fourier's law is adopted as a model of heat conduction

$$\boldsymbol{Q} = -\kappa_c \boldsymbol{C}^{-1} \nabla_0 T \Leftrightarrow \boldsymbol{q} = -\kappa_c \nabla T \,. \tag{70}$$

To reach steady states, accurate modeling of heat-transfer physics in thermomechanical problems requires the adoption of degradation functions for thermal conductivity $\kappa_c$, as shown in [49, 63]. However, the thermal conductivity $\kappa_c$ is assumed constant and independent of $d$ in this study, as our focus lies on analyzing transient rather than steady-state conditions. This assumption may lead to slight inaccuracies in the temperature field around the cracks.

Given the dependence of free energy $\psi$ (Eq. (29)) on the absolute temperature, the total entropy is additively decomposed into elastic, plastic, and thermal components as follows

$$\eta = -\frac{\partial \psi}{\partial T} = \eta^p + \eta^\theta = -\frac{\partial \psi^p}{\partial T} - \frac{\partial \psi^\theta}{\partial T} \,, \tag{71}$$

where the entropy rates can be calculated in a closed form as follows

$$\left.\begin{aligned} \rho_0 T \dot{\eta^p} &= -\left[ T \left( \frac{\partial g^p}{\partial d} \frac{\partial W^p}{\partial T} \right) \dot{d} + T \left( g^p \frac{\partial^2 W^p}{\partial T^2} \right) \dot{T} + T \left( g^p \frac{\partial^2 W^p}{\partial T \partial \bar{\varepsilon}_p} \right) \dot{\bar{\varepsilon}}_p \right] \\ \rho_0 T \dot{\eta^\theta} &= \rho_0 C_v \dot{T} \end{aligned}\right\} \,. \tag{72}$$

Assuming that the contributions of $\dot{d}$, and $\dot{T}$ to the plastic components of entropy are small when the material undergoes extreme plastic deformation, the left-hand side (LHS) of Eq. (69) is approximated by

$$\rho_0 T \dot{\eta} \approx \rho_0 C_v \dot{T} - T \left( g^p \frac{\partial^2 W^p}{\partial T \partial \bar{\varepsilon}_p} \right) \dot{\bar{\varepsilon}}_p \,. \tag{73}$$

Using Eqs. (24), (30), (41) and (44), the generalized dissipative force reads

$$Y_v^p = \rho_0 \frac{\partial \phi^p}{\partial \dot{\bar{\varepsilon}}_p} = g^p(d) \frac{\partial R^p}{\partial \dot{\bar{\varepsilon}}_p} = g^p(d) \left(\sigma_y - \sigma_s\right) = g^p(d) \chi \sigma_y \,, \tag{74}$$

where the Taylor-Quinney (TQ) coefficient [4, 5] is given in closed form as follows

$$\chi = 1 - \frac{\sigma_s}{\sigma_y} = 1 - \sigma_y^{-1} \frac{\partial W^p}{\partial \bar{\varepsilon}_p} \,. \tag{75}$$

Combining the above equations, we arrive at the final form of the governing equation for the temperature

$$\rho_0 C_v \dot{T} = \nabla_0 \cdot \left(\kappa_c \boldsymbol{C^{-1}} \nabla_0 T\right) + Q_p \,, \tag{76}$$

where the heat source resulting from plastic deformation is expressed by

$$Q_p = g^p \left[\chi \sigma_y + T \frac{\partial \sigma_s}{\partial T}\right] \dot{\bar{\varepsilon}}_p \,. \tag{77}$$

In this heat source, significant plastic work heating is attributed to the first term associated with the internal power dissipation density, as described in Eq. (21). In our proposed framework, the closed-form expression for this dissipation density is given by

$$\mathbb{D}^{int} = g^p(d) \chi \sigma_y \dot{\bar{\varepsilon}}_p \,. \tag{78}$$

*Heat flux boundary conditions.* To model the convective heat-transfer processes across the solid-air interface, the following boundary condition for the temperature is applied:

$$q_n = \boldsymbol{q} \cdot \boldsymbol{n} = h_q \left[T(x) - T_\infty\right] \,. \tag{79}$$

In this equation, $q_n$ represents the heat flux in the normal direction, given by the outward unit vector $\boldsymbol{n}$ at the boundary. The material parameter $h_q$ is called heat-transfer coefficient, and the thermal-insulation condition $q_n = 0$ can be employed as a special case when this parameter is set to zero ($h_q = 0$). The term $T(\boldsymbol{x})$ refers to the temperature at the boundary, with $\boldsymbol{x}$ highlighting the dependence on the location of points on the interface where the convective condition is applied. Finally, the parameter $T_\infty$, the so-called far-field temperature, is assumed to be a constant value, typically chosen as the room temperature.

#### *4.2.4. Summary*

In this section, we briefly summarize the elastic-viscoplastic constitutive framework and governing equations, derived in Sections 4.1 and 4.2 respectively.

Table 1: Elastic-viscoplastic constitutive framework

| | |
|---|---|
| Kröner–Lee decomposition: | $\boldsymbol{F} = \boldsymbol{F}^e \boldsymbol{F}^p$ |
| Isochoric assumption: | $J^p = \det\left(\boldsymbol{F}^p\right) = 1 \quad \text{and} \quad J = J^e = \det\left(\boldsymbol{F}^e\right)$ |
| Hyperelastic model: | $\boldsymbol{S} = 2 g^e(d) \boldsymbol{F}^{p\text{-}\mathbf{1}} \left(\frac{\partial W^+}{\partial \boldsymbol{C}^e}\right) \boldsymbol{F}^{p\text{-}\mathbf{T}} + 2 \boldsymbol{F}^{p\text{-}\mathbf{1}} \left(\frac{\partial W^-}{\partial \boldsymbol{C}^e}\right) \boldsymbol{F}^{p\text{-}\mathbf{T}} \quad \text{and} \quad \boldsymbol{\tau} = \boldsymbol{F}\boldsymbol{S}\boldsymbol{F}^{\mathbf{T}}$ |
| Flow rule: | $\boldsymbol{d}^p = \dot{\bar{\varepsilon}}_p \boldsymbol{n}^p \quad \text{where} \quad \boldsymbol{n}^p = \sqrt{\frac{3}{2}} \frac{\boldsymbol{s}}{\|\boldsymbol{s}\|} \quad \text{and} \quad \boldsymbol{s} = \mathbf{dev}\left(\boldsymbol{\tau}\right)$ |
| Viscoplastic flow stress: | $\sigma_y(\bar{\varepsilon}_p, \dot{\bar{\varepsilon}}_p, T) = \sigma_s(\bar{\varepsilon}_p, T) + \sigma_v(\bar{\varepsilon}_p, \dot{\bar{\varepsilon}}_p, T) \quad \text{where} \quad \sigma_s = \frac{\partial W^p}{\partial \bar{\varepsilon}_p} \text{ and } \sigma_v = \frac{\partial R^p}{\partial \dot{\bar{\varepsilon}}_p}$ |
| KKT conditions: | $\widehat{\Phi}_y = \sqrt{\frac{3}{2}} \|\boldsymbol{s}\| - g^p(d) \sigma_y(\bar{\varepsilon}_p, \dot{\bar{\varepsilon}}_p, T) \leq 0 \quad \text{and} \quad \dot{\bar{\varepsilon}}_p \geq 0 \quad \text{and} \quad \widehat{\Phi}_y \dot{\bar{\varepsilon}}_p = 0$ |

Table 2: Governing equations

| | |
|---|---|
| Momentum balance: | $\nabla_0 \cdot (\boldsymbol{F}\boldsymbol{S}) + \rho_0 \bar{\boldsymbol{B}} = \rho_0 \ddot{\boldsymbol{u}}$ |
| Heat equation: | $\rho_0 C_v \dot{T} = \nabla_0 \cdot \left(\kappa_c \boldsymbol{C}^{-1} \nabla_0 T\right) + g^p \left[\chi \sigma_y + T \dfrac{\partial \sigma_s}{\partial T}\right] \dot{\bar{\varepsilon}}_p$ |
| Phase-field equation: | $-G_c \ell_0 \Delta_0 d + \dfrac{G_c}{\ell_0} d + \dfrac{\partial g^e}{\partial d} \mathcal{H}^+ + \dfrac{\partial g^p}{\partial d} \mathcal{H}^p = 0$ |

## 5. Numerical results

In this section, we present four numerical examples to demonstrate the modeling capabilities of the proposed phase-field (PF) fracture framework. We illustrate these capabilities by means of force-displacement curves, field snapshots, and evolution of the variable Taylor-Quinney (TQ) coefficient. All four examples are based on the ductile fracture model described in Section 4 and include thermomechanical coupling with plasticity models that are described by flow stresses for generalized standard materials (see Section 4.1.2).

In Section 5.1, the first example exhibits the ductile failure response of a double-corner-notched square specimen subjected to tensile loading. To study the influence of the location and shape of notches on the failure type, the second example reports the thermomechanical response of a double-edge-notched tension specimen in Section 5.2. In Section 5.3, the third example studies the crack initiation and propagation in an I-shaped specimen, where damage nucleation takes place at the center of the geometry. Finally, in Section 5.4, the fourth example investigates the predictive capabilities of the proposed PF fracture framework by comparing our numerical results to observations and data from the Sandia Fracture Challenge experiment [1].

The first three examples utilize the Johnson-Cook (JC) plasticity model for X30Cr13 stainless steel, while the fourth uses our proposed extended Johnson-Cook (XJC) plasticity model (see Eq. (62)) with a nonlinear hardening law [51] for 15% Chromium - 5% Nickel precipitation hardened (15-5 PH) stainless steel. The evolution of the equivalent plastic strain takes place at the integration points according to the proposed elastic-viscoplastic constitutive framework, reported in Table 1.

Regarding the unknown field variables, the system of three coupled equations, summarized in Table 2, is discretized using the finite element method and implemented in the Multiphysics Object Oriented Simulation Environment (MOOSE) framework [64]. Specifically, we developed a MOOSE-based application to determine the unknown fields: displacement, temperature, and phase-field.

Regarding the implementation details, we employ the Newmark integration scheme for temporal discretization with parameters $\beta = 0.3025$ and $\gamma = 0.6$. The system of governing equations, summarized in Table 2, is solved using a monolithic scheme that is explicit in the phase-field driving forces $\mathcal{H}^+$ and $\mathcal{H}^p$; i.e. at $t = t_{n+1}$, we use the definitions $\mathcal{H}^+ = \max_{t=0,\ldots,t_n} W^+$ and $\mathcal{H}^p = \max_{t=0,\ldots,t_n} W^p$. Lagging the phase-field driving forces by one time increment in this manner improves the performance of the monolithic solver significantly by sidestepping numerical difficulties (singular behavior) associated with non-convexity of the system of coupled equations governing the problem. Several alternative approaches for alleviating this type of numerical difficulties have been described in the literature, including staggered/partitioned and quasi-Newton solution schemes; see [65, 66] and references therein for details.

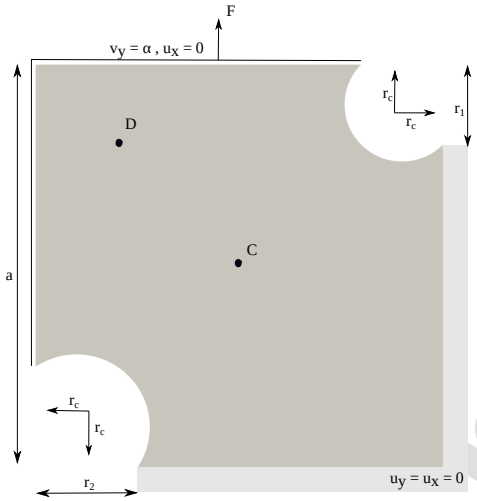


Figure 2: Geometry of the double-corner-notched square specimen, including boundary conditions for displacement and velocity fields.

Finally, an adaptive mesh refinement (AMR) technique, implemented within the MOOSE framework, is used to refine the computational domains in all four examples. The phase-field value serves as the indicator for h-refinement. The initial meshes are created using Cubit [67] with an average element size approximately four times the length scale $\ell_0$. The h-refinement level is set to 3, aiming to achieve a refined mesh size of $h_{ref} = \ell_0/2$. It is noteworthy that AMR can lead to significant CPU savings by refining only the cracked regions, and as a result, it reduces the overall computational cost. Recent studies have demonstrated reductions in computational time by an order of magnitude when using AMR in phase-field fracture simulations [68, 69].

### *5.1. Double-notched square specimen*

In the first example, we examine a double-corner-notched square specimen under combined loading, which leads to shear localization and the formation of a curved crack. The geometry of the sample and its boundary conditions are depicted in Fig. 2, with dimensions $a = 10$ mm, $r_1 = 2$ mm, $r_2 = 2.5$ mm, and $r_c = 1$ mm. In this study, the material parameters for X30Cr13 stainless steel are reported in Table 3 (cf. [70, 71]) unless otherwise specified below. The length scale $\ell_0$ is chosen as 0.03 mm. Initially, the sample is assumed undamaged ($d = 0$) with a uniformly distributed temperature $T_{int}$. With regards to boundary conditions, vertical velocity $v_y$ is applied simultaneously on the top and left edges, while the bottom and right edges are clamped. Convective heat-transfer boundary conditions are imposed as expressed in Eq. (79) with $h_q = 10^{-4}$ W/(mm$^2$K).

To study the performance of the novel plastic degradation function presented in Eq. (47), we first conduct a sensitivity analysis with respect to the parameter $g_f$. Fig. 3 illustrates the influence of $g_f$ on the fracture process in terms of force-displacement curves for $v_y = 10^{-3}$ mm/s and $T_{int} = 294$ K. It is observed that lower values of $g_f$ allow for a greater decrease in the flow stress of the material, which promotes localized plasticity, and hence more pronounced thermal softening and damage accumulation. Together, these effects lead to a total loss of load-carrying capacity of the structure at an earlier stage of deformation. In addition, we perform a sensitivity analysis on $s_0$, the parameter that controls the initial slope (at $d = 0$) of the proposed plastic degradation function. Fig. 4 shows the influence of $s_0$

Table 3: Material properties for X30Cr13 steel and 15-5 PH alloy.

| Material properties | Notation | Values | | Units |
|---|---|---|---|---|
| | | X30Cr13 steel | 15-5 PH alloy | |
| Young's modulus | E | $88.7 \times 10^3$ | $195.0 \times 10^3$ | MPa |
| Poisson's ratio | $\nu$ | 0.34 | 0.3 | - |
| Yield stress | A | 443 | 770 | MPa |
| Ultimate stress | $A^u$ | - | 1250 | MPa |
| Strain hardening modulus | B | 300 | 450 | MPa |
| Saturation parameter | $\delta$ | - | 6 | - |
| Critical energy release rate | $G_c$ | 20.90 | 320 | $kJ/mm^2$ |
| Heat transfer coefficient | $h_q$ | $10^{-4}$ | $10^{-4}$ | $W/mm^2K$ |
| Specific heat capacity | $C_v$ | $0.46 \times 10^9$ | $0.42 \times 10^9$ | $mm^2/(s^2K)$ |
| Thermal conductivity | $\kappa_c$ | 0.038 | 0.0178 | W/mmK |
| Mass density | $\rho_0$ | 7.731 | 7.8 | $g/cm^3$ |
| Thermal softening exponent | q | 1.5 | 1.5 | - |
| Strain rate sensitivity coefficient | C | $6.0 \times 10^{-3}$ | $1.0 \times 10^{-4}$ | - |
| Reference strain rate | $\dot{\bar{\varepsilon}}_0$ | $10^{-4}$ | $10^{-3}$ | $s^{-1}$ |
| Strain hardening exponent | m | 0.7 | 0.7 | - |
| Transition temperature | $T_t$ | 273 | 273 | K |
| Melting temperature | $T_m$ | 1793 | 1713 | K |
| Partial TQ coefficients | $\chi_A = \chi_B$ | 0.95 | 0.99 | - |

on the force-displacement curves for $v_y = 10^{-3}$ mm/s and $T_{int} = 294$ K. It is observed that higher absolute values of $s_0$ result in an earlier onset of loss of load capacity at lower displacements. The residual value $g_f$ and the initial slope $s_0$ of the plastic degradation function in our model achieve a similar effect to the incorporation of a residual plastic energy threshold (e.g. see [35]). In this example, the value of $g_f$ is set to 0.5 and $s_0$ is set to -0.01 unless other values are specified.

Fig. 5 shows a comparison of the force-displacement curves obtained from our formulation (for $v_y = 10^{-3}$ mm/s, $T_{int} = 294$ K, and $g_f = 0.7$) with other numerical approaches published in the literature. In [43], a ductile fracture model was developed that incorporates a modified elastic degradation function dependent on both the phase-field variable and the accumulated plastic strain. In [70], a non-local softening model was employed to capture the localization of plastic behavior. In comparison to these approaches, our results are similar to those of [43] in terms of the higher overall load-carrying capacity up to $u_y \approx 0.15$ mm, and they also exhibit a softening behavior similar to that of [70] with continued deformation up to failure at $u_y \approx 0.4$ mm. In general, our results also reflect lower ductility in comparison to these two other models.

The influence of temperature on the mechanical behavior of the double-notched square specimen is examined by

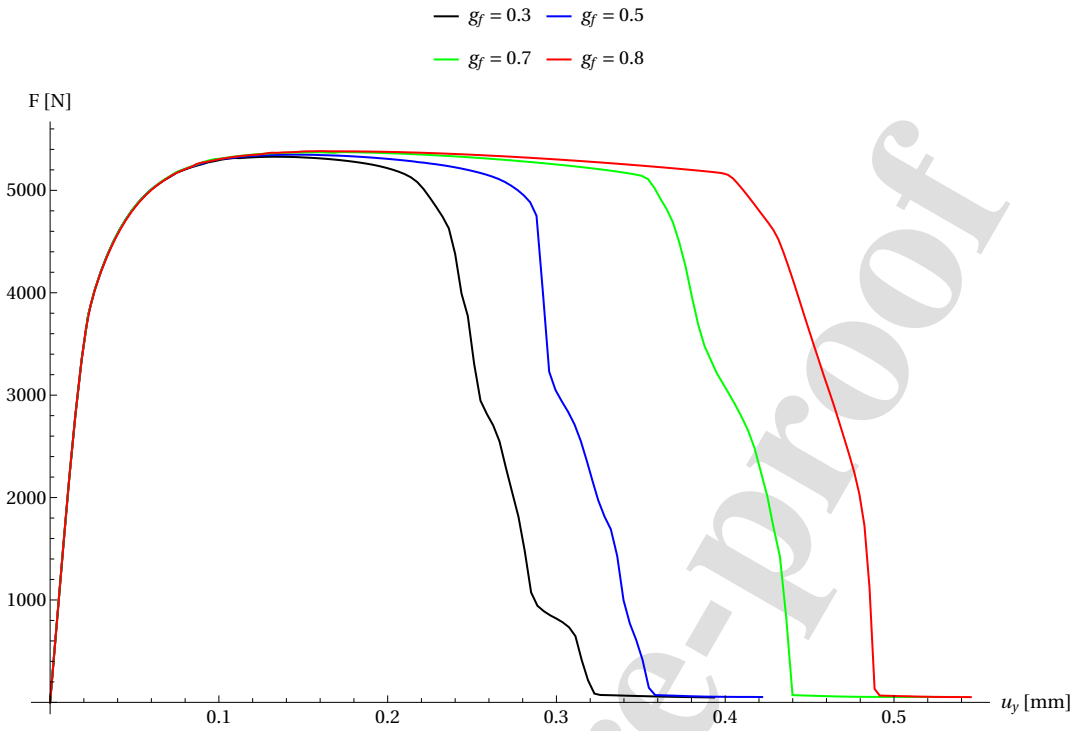


Figure 3: Influence of $g_f$ on the force-displacement curves in the double-notched square specimen. The initial temperature is $T_{int} = 294$ K and the loading rate is given by $v_y = 10^{-3}$ mm/s.

varying the initial temperature values $T_{int}$. Specifically, we conduct simulations with four $T_{int}$ values: 294 K, 400 K, 600 K, and 800 K, while the far-field temperature is maintained at room temperature ($T_\infty = 294$ K). The temperature effect is shown in Fig. 6, where higher $T_{int}$ values reduce the peak force $F$ and delay crack initiation.

The influence of the loading rate on the response of the double-notched square specimen is investigated using four different $v_y$ values: $10^{-3}$ mm/s, $10^{-2}$ mm/s, 0.05 mm/s, and 0.1 mm/s. Fig. 7 shows that higher loading rates result in an increase in the peak force $F$, indicating that the specimen can withstand greater forces before failure (due to strain-rate hardening effects). However, higher loading rates do not necessarily lead to earlier failure. For instance, the peak load for $v_y = 10^{-2}$ mm/s is found to be higher compared to $v_y = 10^{-3}$ mm/s. Nevertheless, failure happens at lower displacements for $v_y = 10^{-2}$ mm/s. A similar trend is observed when comparing $v_y = 0.05$ mm/s and $v_y = 0.1$ mm/s. However, the peak load for $v_y = 0.1$ mm/s is higher, and failure occurs at higher displacements compared to the case with $v_y = 10^{-3}$ mm/s. It is important to note that Fig. 7 presents the overall structural response of the specimen, and not the local response at a material point. This structural response stems from the complex interplay between various nonlinear, coupled processes at the level of each material point, in addition to nonlinear geometric effects and local instabilities (such as shear bands) which can significantly affect global deformation and failure modes. It is therefore difficult to disentangle these mechanisms in order to explain the overall response and/or attribute individual aspects of that response to a particular mechanism. This underscores the importance of accounting for the coupling between thermomechanics and damage, to the fullest possible extent, when studying ductile fracture problems.

Snapshots showing the crack formation and plastic localization are depicted in Figs. 8 and 9 respectively. For the

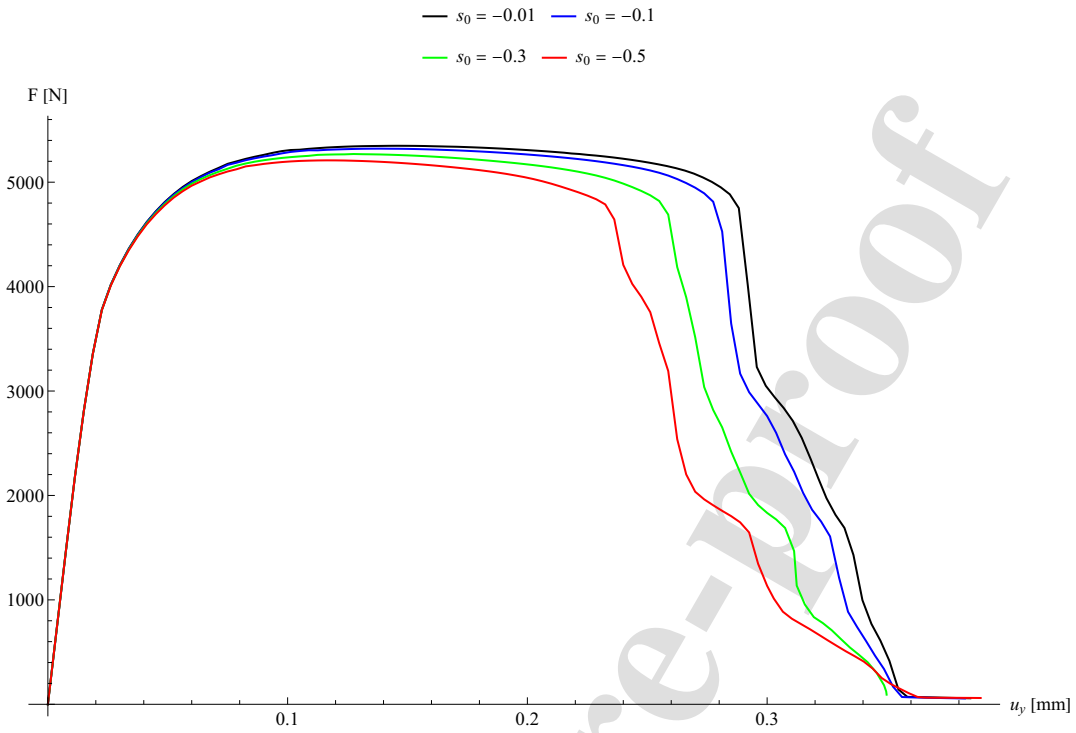


Figure 4: Influence of $s_0$ on the force-displacement curves in the double-notched square specimen. The initial temperature is $T_{int}$ = 294 K and the loading rate is given by $v_y = 10^{-3}$ mm/s.

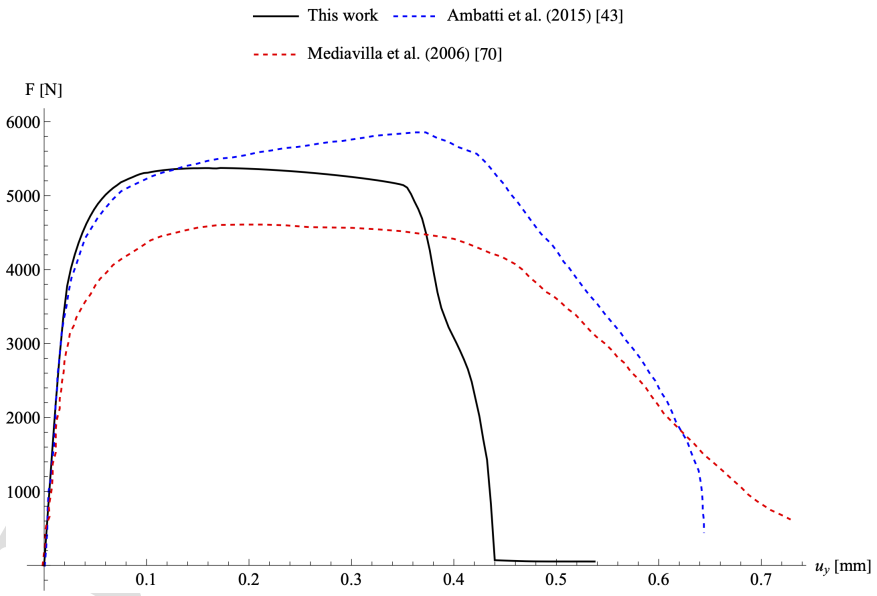


Figure 5: A comparison of the load–displacement curves between our formulation and the approaches from Ambati *et al.* (2015) [43] and Mediavilla *et al.* (2006) [70] in the double-notched square specimen. The initial temperature is $T_{int}$ = 294 K and the loading rate is given by $v_y = 10^{-3}$ mm/s with $s_0$ = -0.01 and $g_f$ = 0.7.

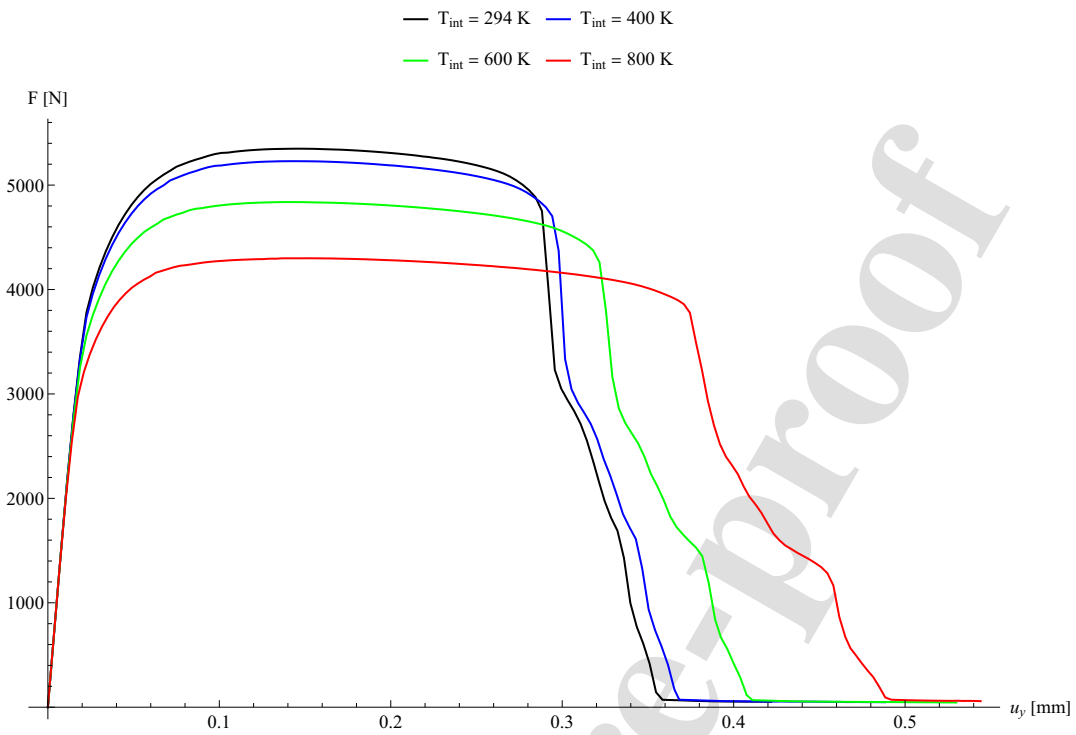


Figure 6: Influence of four different initial temperatures on the mechanical behavior of the double-notched square specimen, illustrated by the corresponding force-displacement curves. The loading rate is $v_y = 10^{-3}$ mm/s.

loading rate of $v_y = 0.1$ mm/s and initial temperature of $T_{int} = 294$ K, we illustrate the evolution of the phase-field variable (Fig. 8) and the equivalent plastic strain (Fig. 9) for six time steps with vertical displacements $u_y$ of (a) 0.265 mm, (b) 0.298 mm, (c) 0.305 mm, (d) 0.309 mm, (e) 0.357 mm, and (f) 0.391 mm (as indicated by the corresponding letters in Fig. 7). It is observed that a curved crack develops on top of a plastic localization zone, which nucleates close to the notches. Figs. 10 and 11 show the evolution of the temperature field and the internal power dissipation density (expressed in Eq. (78)) at the same time steps, with identical initial and boundary conditions ($T_{int} = 294$ K and $v_y = 0.1$ mm/s).

Next, we study the fraction of plastic work converted into heat when the JC plasticity model of Eq. (61) is applied. Fig. 12 illustrates the evolution of the Taylor-Quinney (TQ) coefficient $\chi$ (defined in Eq. (75)) over time at two material points and four different loading rates. As both depicted in Fig. 2, point C is located at (5.4 mm, 5.15 mm), i.e. inside the expected crack path, whereas Point D, with coordinates (2 mm, 8 mm), lies outside this path. The results are obtained with four imposed velocities $v_y$ of 0.1 mm/s, 5 mm/s, 100 mm/s and 500 mm/s, along with initial temperature of $T_{int} = 294$ K and coefficients $\chi_A = \chi_B = 0.8$. It is observed that the TQ coefficient has approximately the same value with $\chi_A$ and $\chi_B$ at Point D (outside the crack path). On the other hand, the TQ coefficient at Point C (within the crack path) increases as fracture propagates and returns to the values of $\chi_A$ and $\chi_B$ after the complete crack formation. The maximum values of the TQ coefficient at Point C slightly increase with higher loading rates. In the context of generalized standard materials using the JC plasticity model as expressed by Eq. (61), the sensitivity of the TQ coefficient to loading rates is less than 2%. If the TQ coefficient were (hypothetically) highly dependent on the

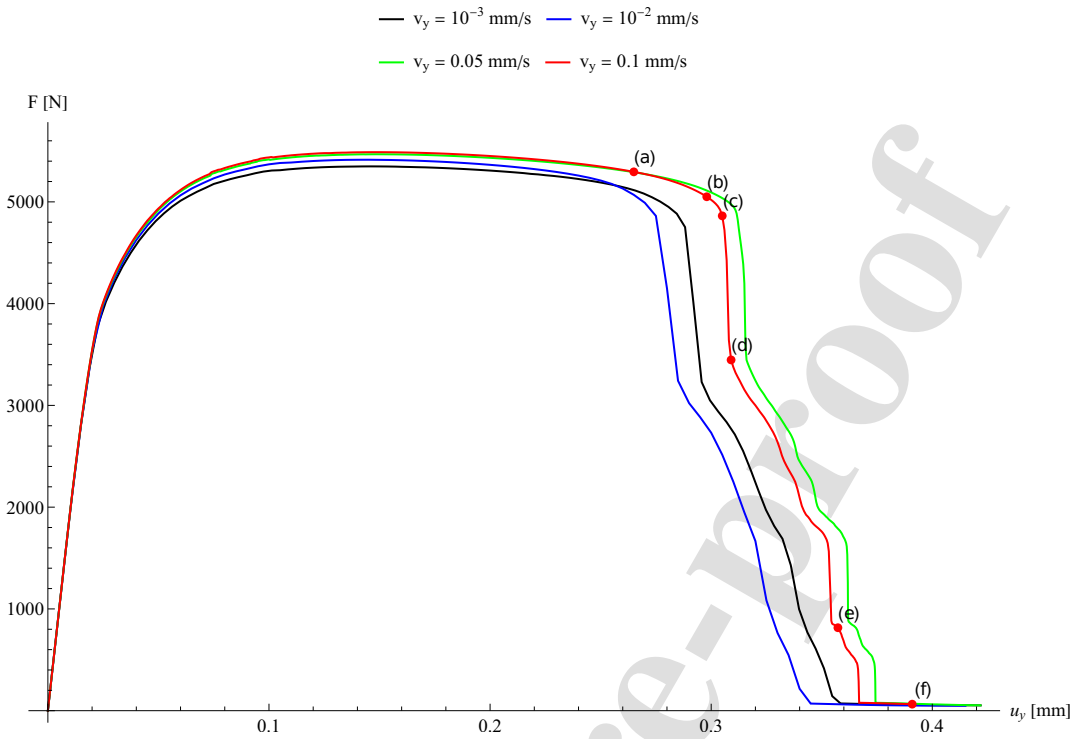


Figure 7: Influence of the loading rate on the response of the double-notched square specimen, investigated using four different prescribed velocities. The initial temperature is assumed $T_{int} = 294$ K.

loading rate, a different plasticity model could be adopted by introducing alternative functions for the stored energy density due to plastic work and the dissipation pseudo-potential (see Section 4.1.2).

In the proposed framework, plastic work heating depends on the plastic degradation function $g^p$ as expressed in Eq. (77). This coupling prevents the temperature from rising excessively after damage initiation. To study this effect, we conduct two analyses: one with a degraded heat source and one without. The results are obtained for initial temperature $T_{int} = 800$ K, imposed velocity $v_y = 5$ mm/s, and coefficients $\chi_A = \chi_B = 0.8$. Fig. 13 shows that neglecting the effects of damage on the heat equation can lead to higher local temperatures, albeit without significantly affecting the load-displacement curve in this case. Specifically, the evolution of temperature fields at Point C is presented in Fig. 13a. It illustrates that as the crack propagates, the maximum temperature at Point C reaches about 970 K when the heat source is degraded, whereas the peak temperature is approximately 1080 K when it is not degraded. As a result, the increase in temperature leads to a slightly earlier loss of load-bearing capacity, as observed in Fig. 13b, in accordance with the thermal effects predicted by the JC plasticity model.

Finally, we examine the mesh convergence behavior by testing three different cases of AMR refinement levels: $h_{ref} = 2$, 3, and 4. The results are compared to the non-AMR case, where the mesh is pre-refined along the crack path with a minimum mesh size of $h = \ell_0/4$. Fig. 14a shows that mesh convergence is achieved for $h_{ref} = 3$ and 4, as there is no significant difference in the force-displacement curves for these cases compared to the non-AMR case (up to point D). After point D, the two cracks merge into one, causing the specimen to fully fracture. This process occurs rapidly and requires elements in the middle of the specimen to be refined quickly. The AMR mesh with $h_{ref} = 3$

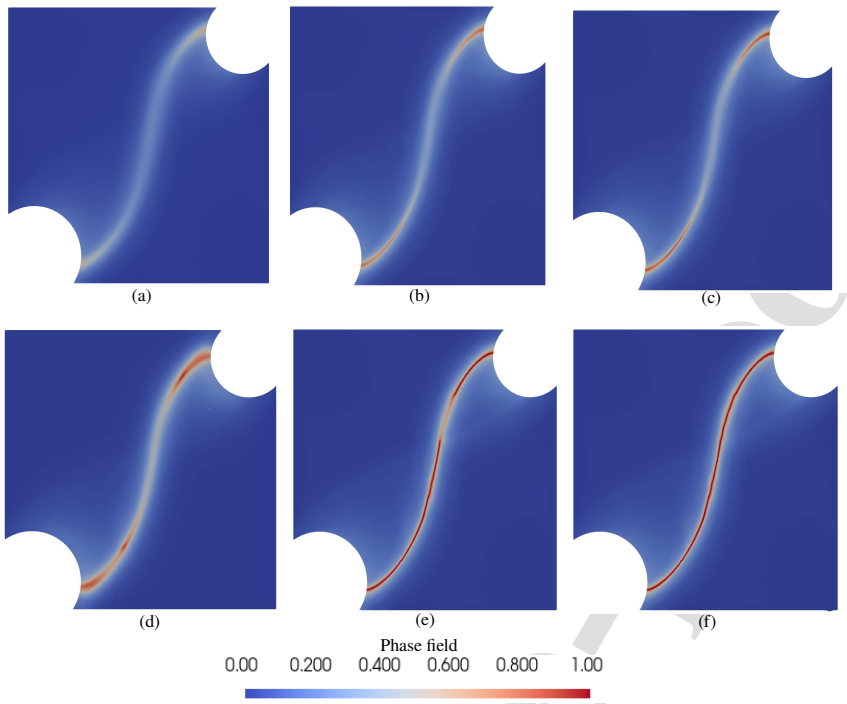


Figure 8: Snapshots showing the phase-field evolution at six time steps with vertical displacements $u_y$ of (a) 0.265 mm, (b) 0.298 mm, (c) 0.305 mm, (d) 0.309 mm, (e) 0.357 mm, and (f) 0.391 mm (as indicated by the letters in Fig. 7). The results are obtained with an initial temperature of $T_{int}$ = 294 K and a loading rate of $v_y$ = 0.1 mm/s.

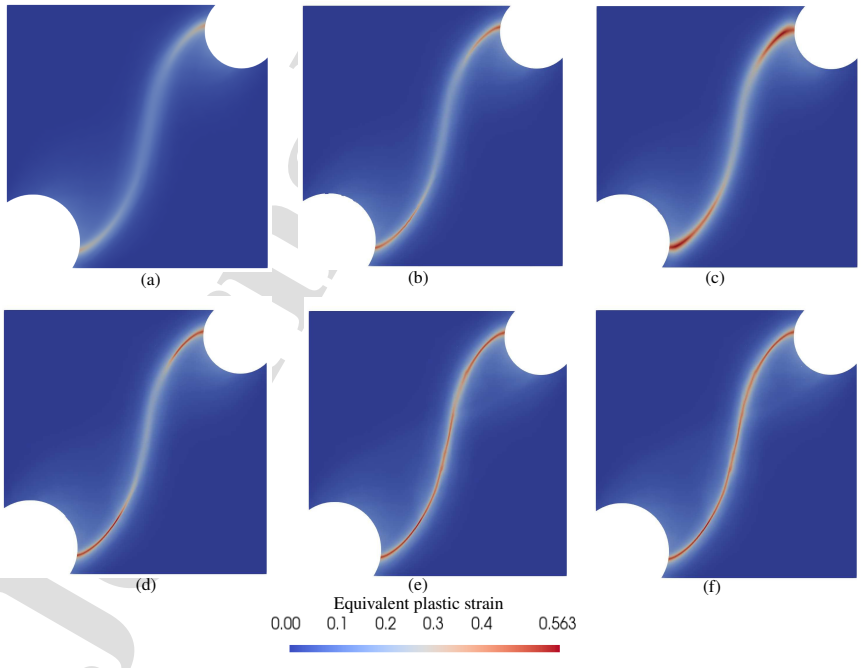


Figure 9: Snapshots showing the evolution of the equivalent plastic strain at six time steps with vertical displacements $u_y$ of (a) 0.265 mm, (b) 0.298 mm, (c) 0.305 mm, (d) 0.309 mm, (e) 0.357 mm, and (f) 0.391 mm (as indicated by the letters in Fig. 7). The results are obtained with an initial temperature of $T_{int}$ = 294 K and a loading rate of $v_y$ = 0.1 mm/s.

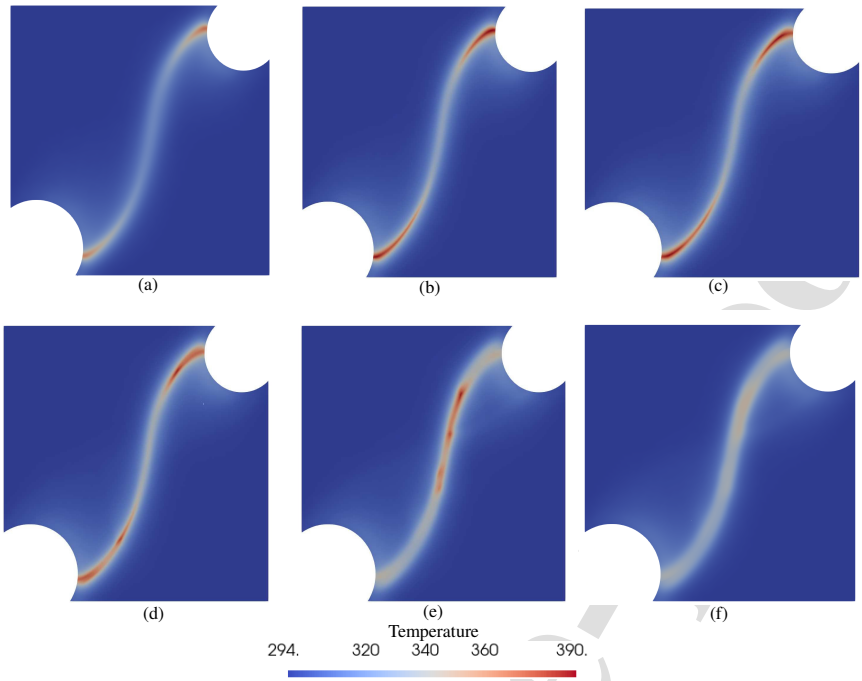


Figure 10: Snapshots showing the temperature evolution at six time steps with vertical displacements $u_y$ of (a) 0.265 mm, (b) 0.298 mm, (c) 0.305 mm, (d) 0.309 mm, (e) 0.357 mm, and (f) 0.391 mm (as indicated by the letters in Fig. 7). The results are obtained with an initial temperature of $T_{int} = 294$ K and a loading rate of $v_y = 0.1$ mm/s.

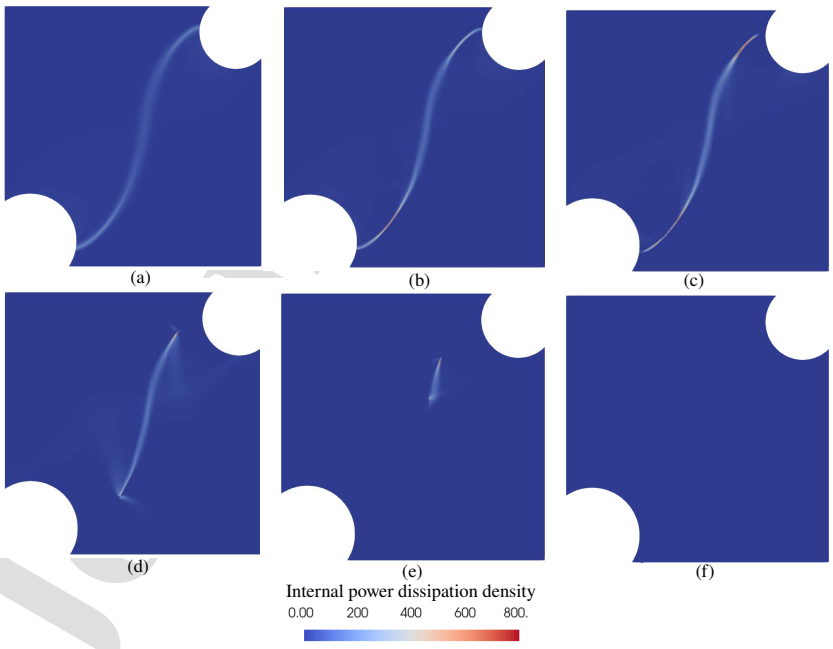


Figure 11: Snapshots showing the evolution of the internal power dissipation density at six time steps with vertical displacements $u_y$ of (a) 0.265 mm, (b) 0.298 mm, (c) 0.305 mm, (d) 0.309 mm, (e) 0.357 mm, and (f) 0.391 mm (as indicated by the letters in Fig. 7). The results are obtained with an initial temperature of $T_{int} = 294$ K and a loading rate of $v_y = 0.1$ mm/s.

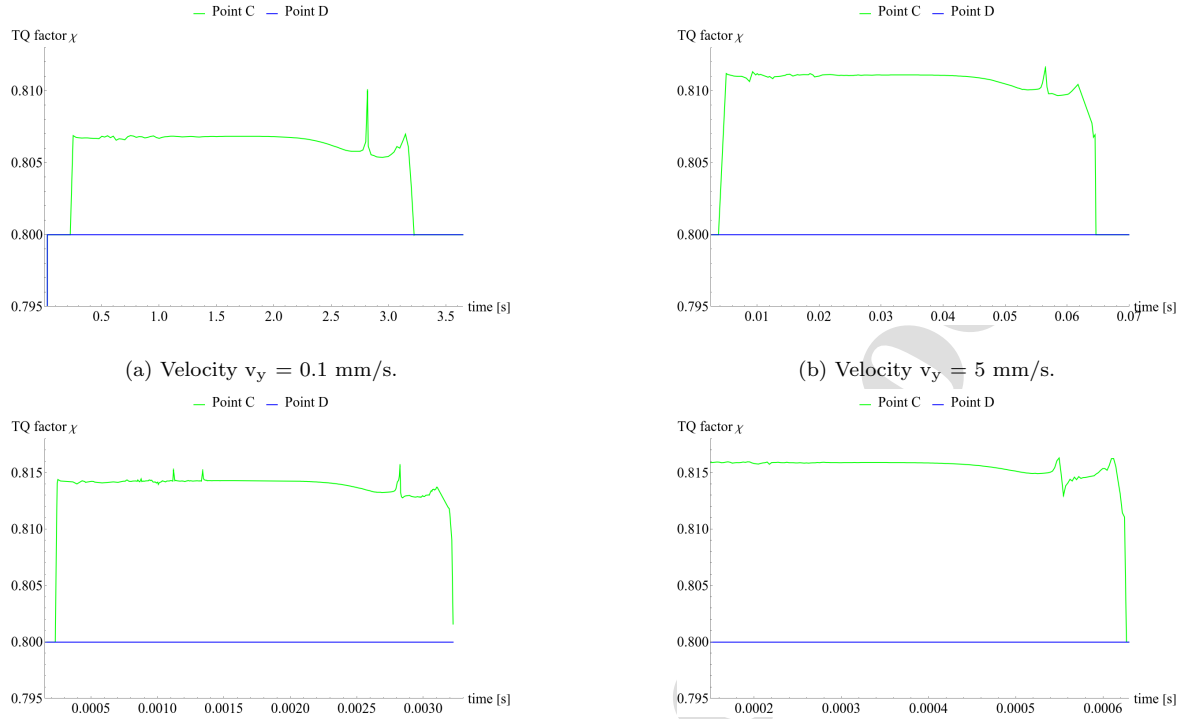


(a) Velocity $v_y = 0.1$ mm/s.

(b) Velocity $v_y = 5$ mm/s.

(c) Velocity $v_y = 100$ mm/s.

(d) Velocity $v_y = 500$ mm/s.

Figure 12: The influence of loading rates on the TQ coefficient.

lags behind those with $h_{\text{ref}} = 4$ and the pre-refined mesh in capturing this phenomenon. However, capturing the force-displacement curve beyond point D is also extremely challenging in experiments with ductile materials. Fig. 14b illustrates the evolution of the degrees of freedom (DOFs) with respect to increasing applied displacement. We observe that the computational cost of AMR with $h_{\text{ref}} = 3$ is significantly reduced compared to the non-AMR case before crack initiation, and compared to AMR with $h_{\text{ref}} = 4$ after crack propagation, respectively. Considering both computational efficiency and accuracy, we determine that AMR with $h_{\text{ref}} = 3$ is the optimal choice for our model.

### *5.2. Double-edge-notched tension specimen*

In the second example, a double-edge-notched tension (DENT) specimen with U-shaped notches is examined. This problem is experimentally investigated in [72]. The specimen's geometry and boundary conditions are depicted in Fig. 15, with dimensions a = 47 mm, b = 25 mm, $r_c$ = 2.5 mm, and h = 8 mm. In this study, the material parameters for X30Cr13 stainless steel are reported in Table 3 unless otherwise specified below. The length scale $\ell_0$ is 0.03 mm, and the value of $g_f$ is selected to be 0.5 in this problem. Regarding the initial and boundary conditions, the sample is considered undamaged (i.e., $d = 0$) with a uniformly distributed temperature denoted by $T_{\text{int}}$. The bottom edge is clamped, while the top edge is subjected to a vertical velocity $v_y$. Convective heat-transfer boundary conditions are imposed as expressed in Eq. (79) with $h_q = 10^{-4}$ W/(mm$^2$K).

Fig. 16 illustrates the influence of temperature on the mechanical behavior of the DENT specimen by varying the initial temperature values $T_{\text{int}}$. Specifically, we conduct four simulations with the following values of $T_{\text{int}}$: 294 K, 400 K, 600 K, and 800 K. The far-field temperature is maintained at room temperature (i.e., $T_\infty = 294$ K), and the

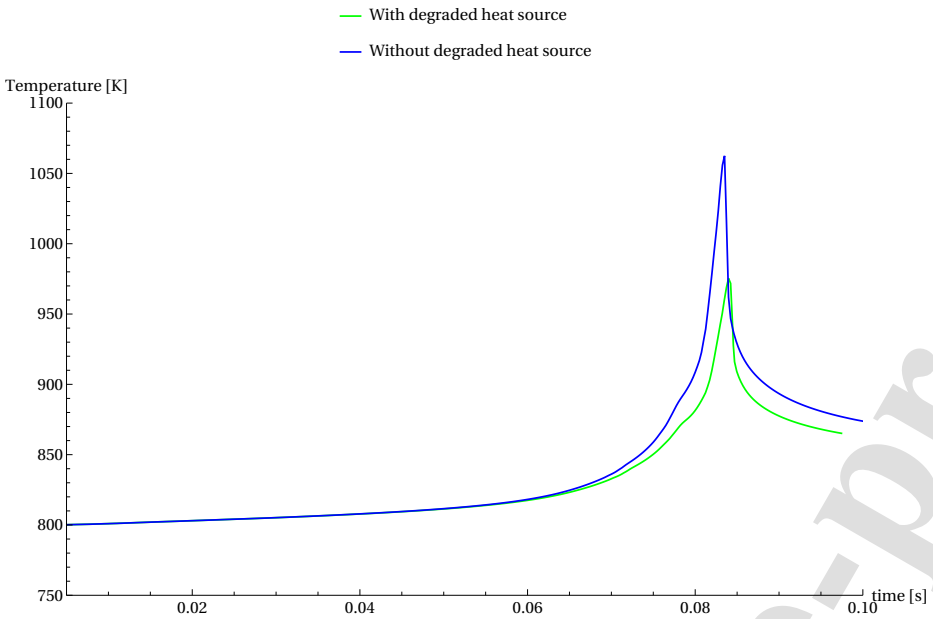


(a) Evolution of temperature fields at Point C for analyses with different heat source terms. Neglecting the effects of damage on the heat equation can lead to higher local temperatures.

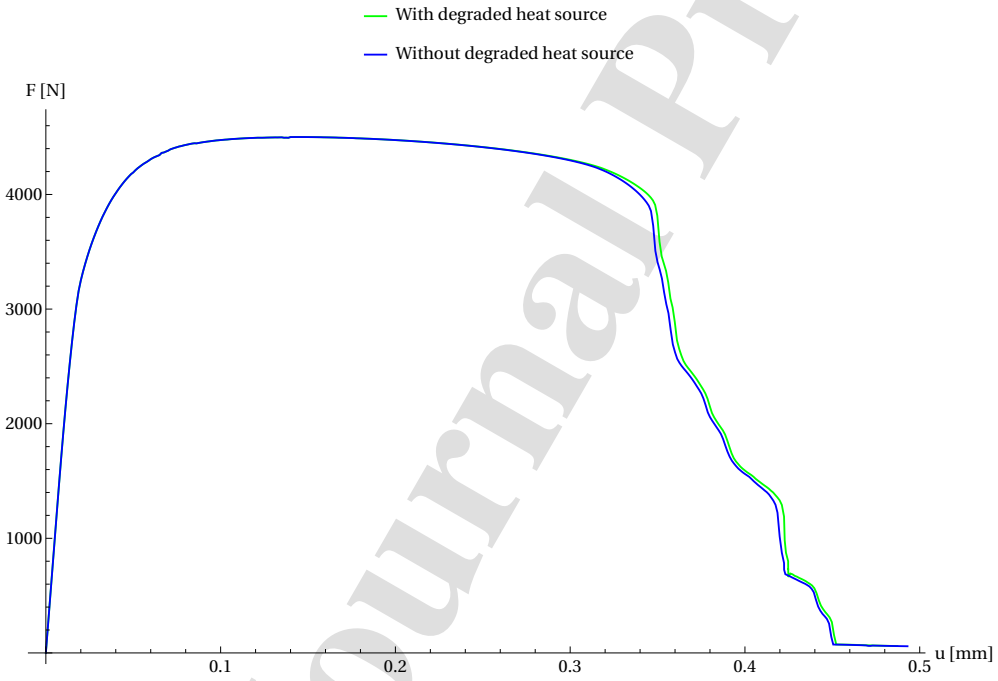


(b) Force-displacement curves for analyses with different heat source terms. The increase in temperature leads to a slightly earlier loss of load-bearing capacity.

Figure 13: The influence of damage on the thermomechanical coupling. Two analyses are conducted: one with a degraded heat source due to the plastic degradation function and one without. The results are obtained for initial temperature $T_{int}$ = 800 K, imposed velocity $v_y$ = 5 mm/s, and coefficients $\chi_A = \chi_B = 0.8$.

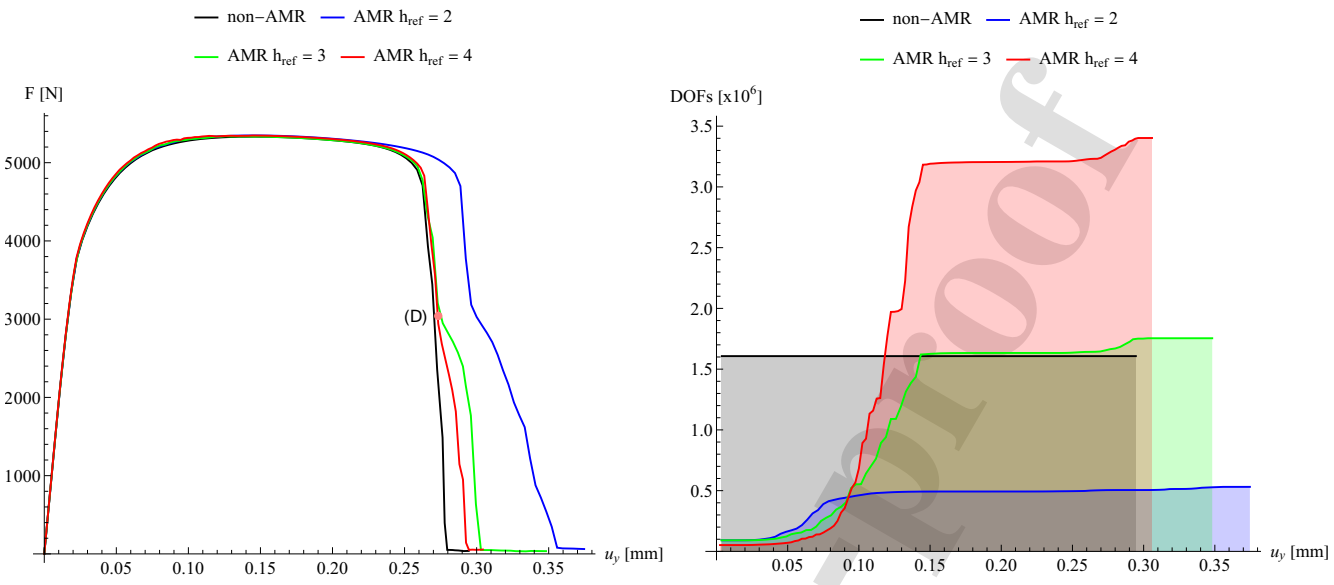


(a) Force-displacement curves.

(b) Evolution of DOFs.

Figure 14: Double-notched square specimen: (a) Mesh convergence studies for different AMR refinement levels $h_{ref}$ compared to the non-AMR case. (b) The evolution of degrees of freedom (DOFs) with respect to increasing applied displacements $u_y$ shows that $h_{ref} = 3$ is the optimal choice for our model.

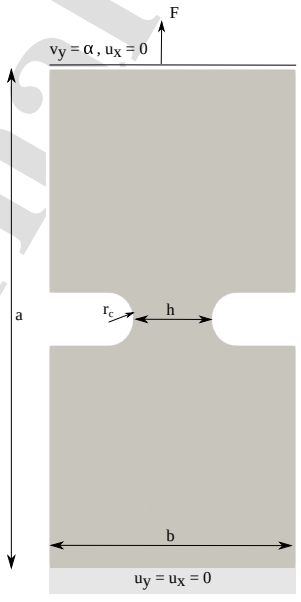


Figure 15: Geometry of the DENT specimen, including boundary conditions for displacement and velocity fields.

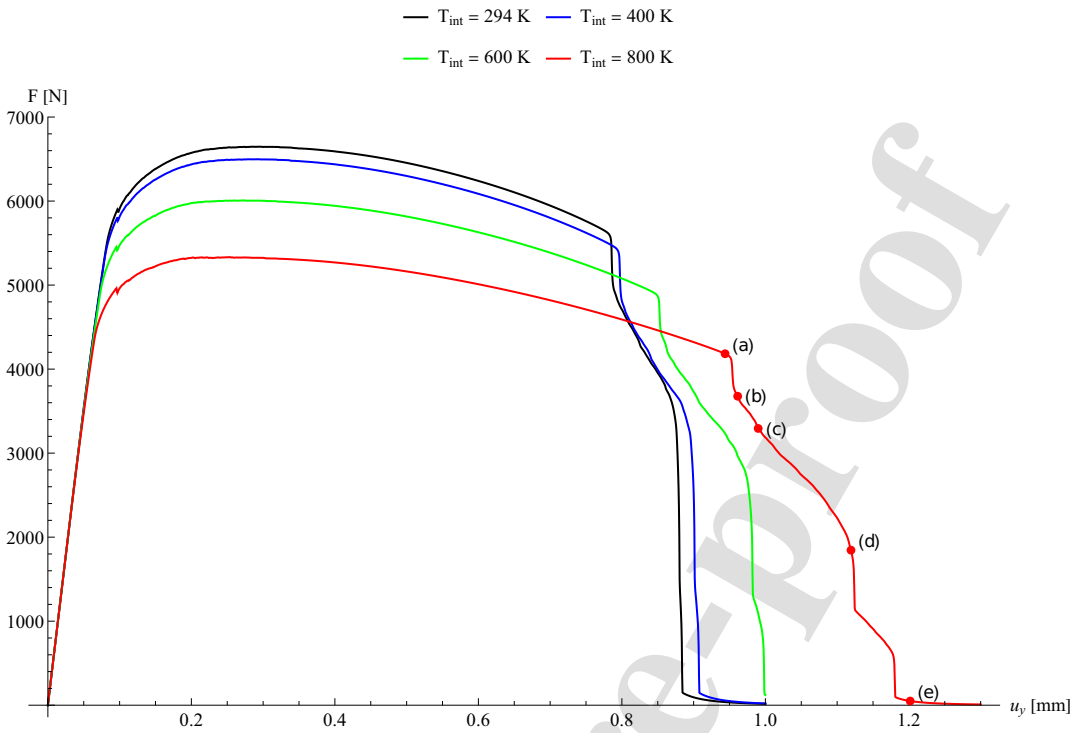


Figure 16: Influence of four different initial temperatures on the mechanical behavior of the DENT specimen, illustrated by the corresponding force-displacement curves. The loading rate is governed by the prescribed velocity of $v_y = 0.1$ mm/s.

imposed loading rate is governed by the prescribed velocity of $v_y = 0.1$ mm/s. Similar to the previous example, higher $T_{int}$ values reduce the peak force $F$ in the force-displacement curves but increase ductility by delaying the complete loss of load-bearing capacity.

However, the dependence of the specimen's load-bearing capacity on the deformation rate does not follow the same pattern as reported in the previous example. Specifically, Fig. 17 shows the force-displacement curves for various loading rates imposed by prescribed velocities of $v_y = 10^{-3}$ mm/s, $10^{-2}$ mm/s, and $10^{-1}$ mm/s; and it is observed that fracture occurs at monotonically higher values of displacement with increasing loading rates. This structural response is due to both the geometry of the specimen and the coupled local material processes. Thus, even though the response follows a different (and perhaps, more intuitive) trend compared to the previous case, this trend is equally difficult to predict without accounting for all the relevant physical mechanisms and the coupling between them.

Snapshots showing the crack propagation and plastic deformation are depicted in Figs. 18 and 19. For the imposed velocity of $v_y = 0.1$ mm/s and initial temperature of $T_{int} = 800$ K, we illustrate the evolution of the phase-field variable (Fig. 18) and the equivalent plastic strain (Fig. 19) for five time steps with vertical displacements $u_y$ of (a) 0.944 mm, (b) 0.961 mm, (c) 0.990 mm, (d) 1.119 mm, and (e) 1.202mm (as indicated by the corresponding letters in Fig. 16). It is observed that a crack forms on top of the two plastic localization zones, which develop between the U-shaped notches. It is also worth noting that one branch of the X-shaped crack develops faster than the other due to small numerical errors and/or slight mesh asymmetry. Figs. 20 and 21 show the evolution of the temperature field and the internal power dissipation density (expressed in Eq. (78)) at the same time steps, with identical initial and boundary

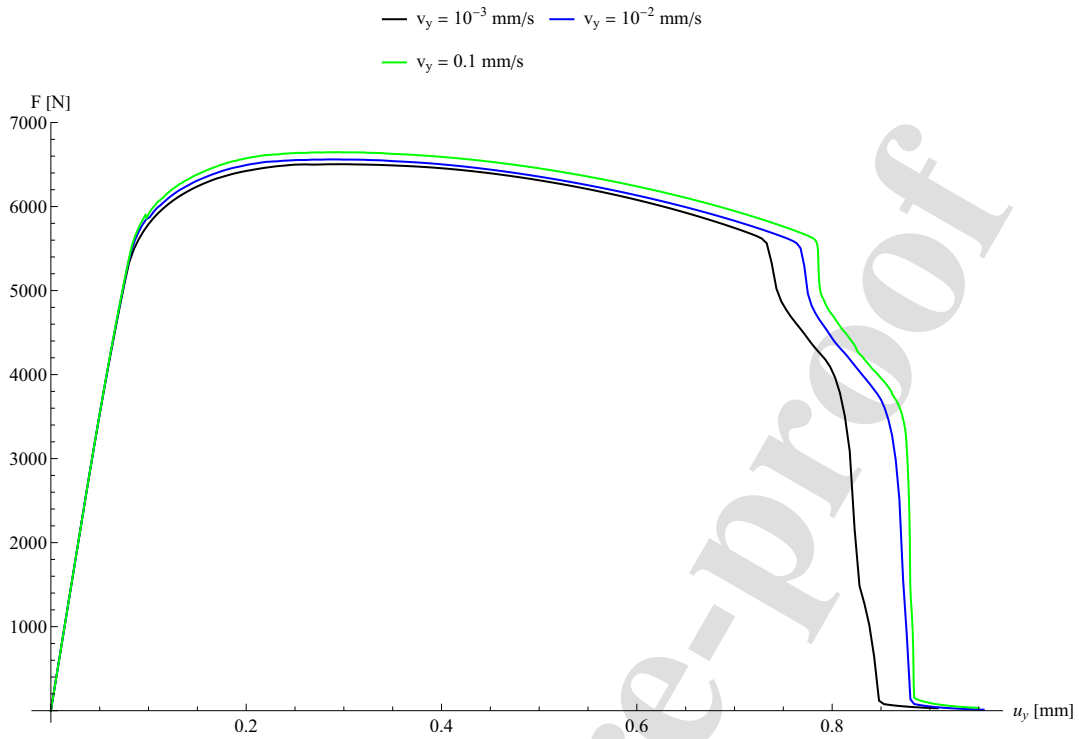


Figure 17: Influence of loading rates on the response of the DENT specimen, investigated using three different prescribed velocities. The initial temperature is assumed $T_{int}$ = 294 K.

conditions ($v_y$ = 0.1 mm/s and $T_{int}$ = 800 K).

### *5.3. I-shaped specimen*

In the third example, we examine an I-shaped specimen subjected to tensile loading. The geometry of the sample and its boundary conditions are depicted in Fig. 22, where the dimensions are given as L = 14 mm, b = 6 mm, c = 4 mm, and $r_c$ = 1 mm. This configuration is a scaled version of an example presented in [43]. Scaling the geometry of the sample allows the use of the same length scale as in the previous example at a reasonable computational cost. Similar to the previous two examples, the material parameters for X30Cr13 stainless steel are listed in Table 3, unless otherwise stated below. The length scale $\ell_0$ is selected to be 0.03 mm, and the value of $g_f$ is set to 0.5 in this problem. Regarding the initial and boundary conditions, the sample is assumed to be undamaged with a uniformly distributed initial temperature denoted by $T_{int}$ in the numerical studies, while vertical velocities $v_y$ are applied to the top and bottom edges (Fig. 22). Convective heat-transfer boundary conditions are imposed as expressed in Eq. (79) with $h_q = 10^{-4}$ W/(mm$^2$K).

Fig. 23 illustrates the effect of temperature on the mechanical behavior of the I-shaped specimen by varying the initial temperature $T_{int}$. To this end, we conduct four analyses with the following values of $T_{int}$: 294 K, 400 K, 600 K and 800 K. The far-field temperature remains $T_\infty = 294K$ (room temperature), and the loading rate is controlled by the prescribed velocity $v_y = 10^{-3}$ mm/s. Similar to the previous examples, it is observed that higher initial temperature values $T_{int}$ reduce the peak force $F$ in the force-displacement curves but increase ductility by delaying the complete

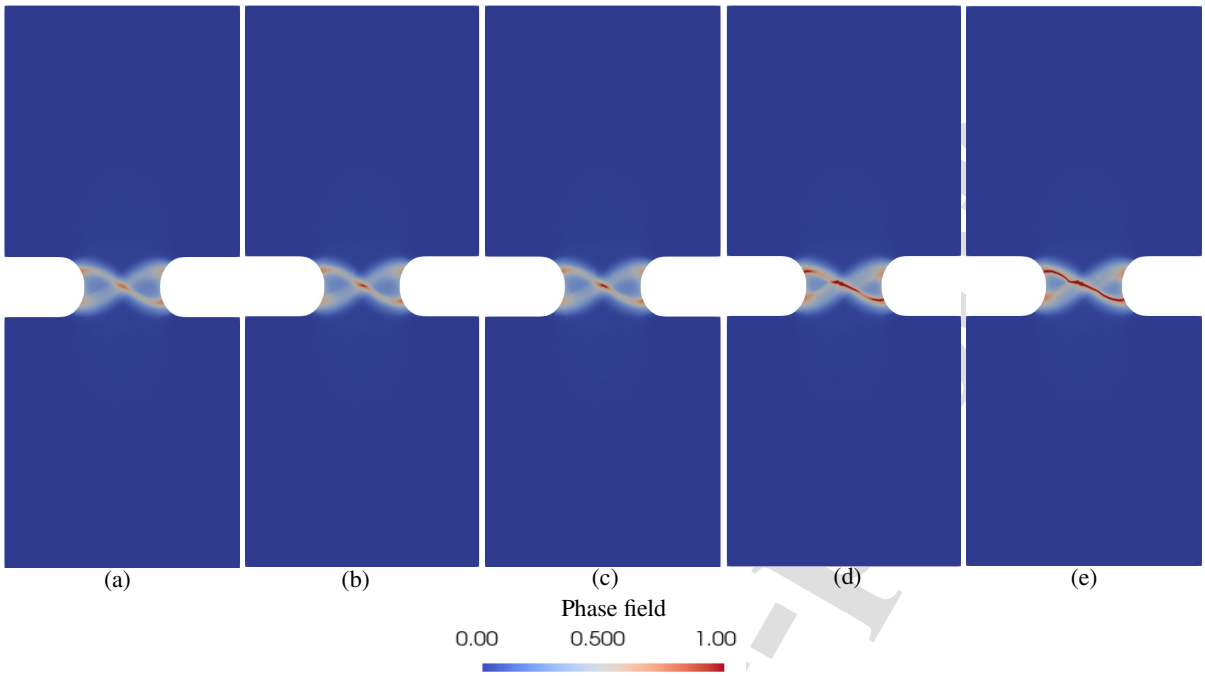


Figure 18: Snapshots showing the phase-field evolution at five time steps with vertical displacements $u_y$ of (a) 0.944 mm, (b) 0.961 mm, (c) 0.990 mm, (d) 1.119 mm, and (e) 1.202mm (as indicated by the corresponding letters in Fig. 16). The results are obtained with an initial temperature of $T_{int}$ = 800 K and a loading rate imposed by the prescribed velocity of $v_y$ = 0.1 mm/s.

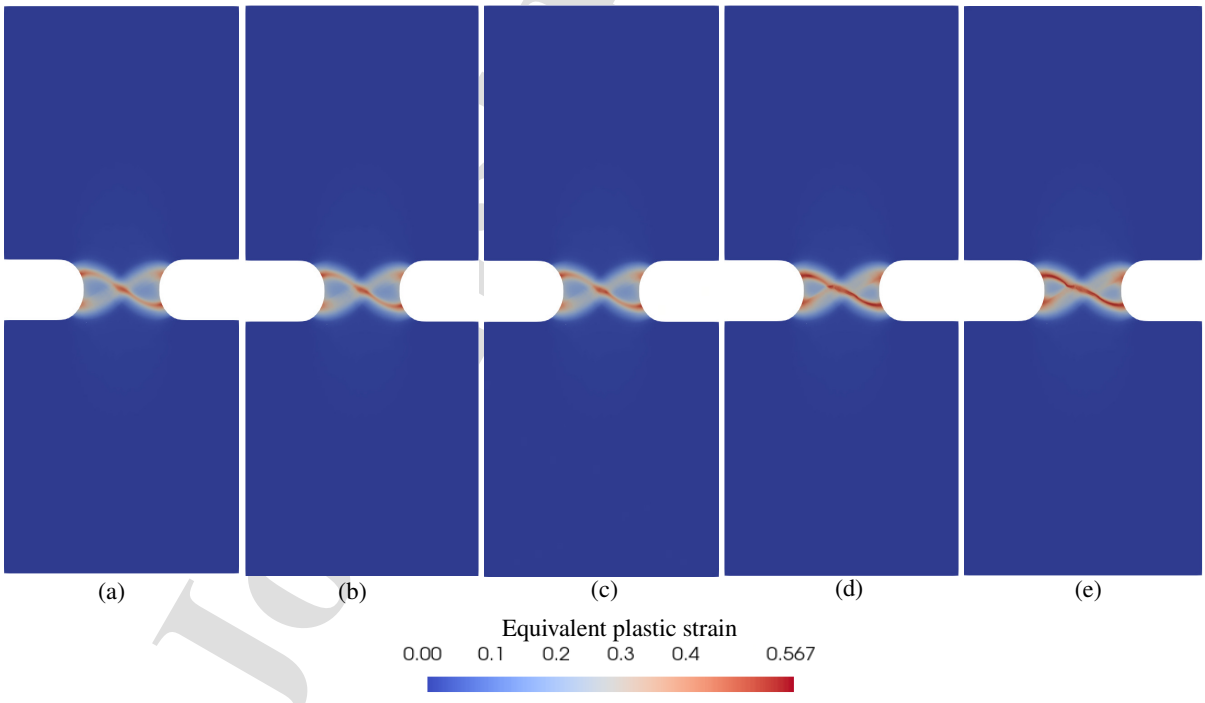


Figure 19: Snapshots showing the evolution of the equivalent plastic strain at five time steps with vertical displacements $u_y$ of (a) 0.944 mm, (b) 0.961 mm, (c) 0.990 mm, (d) 1.119 mm, and (e) 1.202mm (as indicated by the corresponding letters in Fig. 16). The results are obtained with an initial temperature of $T_{int}$ = 800 K and a loading rate imposed by the prescribed velocity of $v_y$ = 0.1 mm/s.

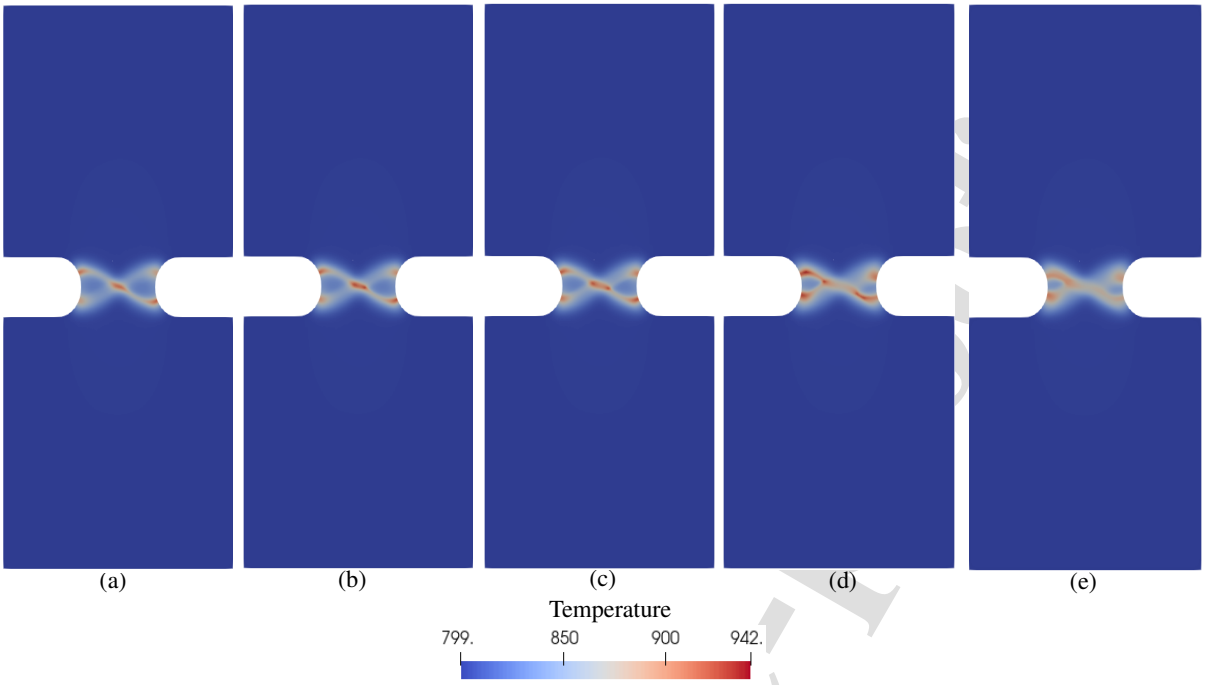


Figure 20: Snapshots showing the temperature evolution at five time steps with vertical displacements $u_y$ of (a) 0.944 mm, (b) 0.961 mm, (c) 0.990 mm, (d) 1.119 mm, and (e) 1.202mm (as indicated by the corresponding letters in Fig. 16). The results are obtained with an initial temperature of $T_{int} = 800$ K and a loading rate imposed by the prescribed velocity of $v_y = 0.1$ mm/s.

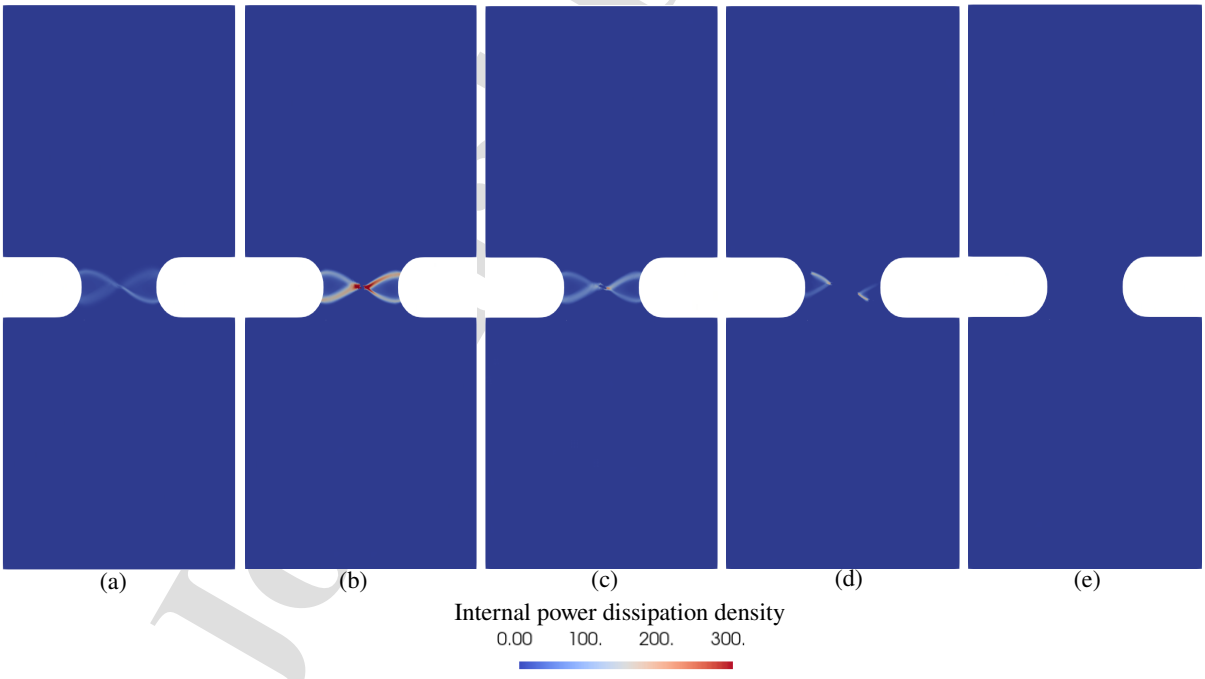


Figure 21: Snapshots showing the evolution of the internal power dissipation density at five time steps with vertical displacements $u_y$ of (a) 0.944 mm, (b) 0.961 mm, (c) 0.990 mm, (d) 1.119 mm, and (e) 1.202mm (as indicated by the corresponding letters in Fig. 16). The results are obtained with an initial temperature of $T_{int} = 800$ K and a loading rate imposed by the prescribed velocity of $v_y = 0.1$ mm/s.

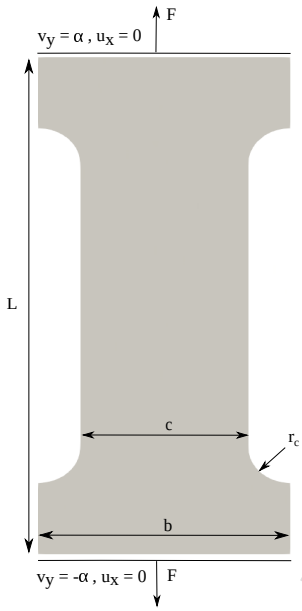


Figure 22: Geometry of the I-shaped specimen, including boundary conditions for displacement and velocity fields.

loss of load-bearing capacity.

The dependence of the specimen's failure on imposed loading rates is studied in Fig. 24. We observe that higher loading rates result in an increase in the peak load in force-displacement curves due to strain-rate hardening effects. In addition, the displacement at failure decreases with increasing loading rates in this example. This is the opposite of the trend observed in the previous example. However, it can be considered the most intuitive trend compared to the two previous examples, given the simplicity of the specimen geometry and loading conditions in the present case.

Snapshots showing the crack propagation and plastic deformation prior to failure are depicted in Figs. 25 and 26. For the imposed velocity of $v_y = 0.1$ mm/s and initial temperature $T_{int} = 294$ K, we plot the evolution of the phase-field variable (Fig. 25) and the equivalent plastic strain (Fig. 26) for six time steps with vertical displacements $u_y$ of (a) 0.359 mm, (b) 0.400 mm, (c) 0.415 mm, (d) 0.426 mm, (e) 0.429 mm, and (f) 0.452 mm (as indicated by the corresponding letters in Fig. 24). It is observed that crack nucleation occurs at the center of the specimen, where plastic deformation is most extensive. After crack initiation, it propagates along the plastic localization zones. Figs. 27 and 28 show the evolution of temperature fields and the internal power dissipation density (expressed in Eq. (78)) at the aforementioned time steps, with identical initial and boundary conditions ($T_{int} = 294$ K and $v_y = 0.1$ mm/s).

### *5.4. Sandia Fracture Challenge*

In the fourth example, we assess the predictive capabilities of the proposed PF fracture framework by comparing our numerical results to experimental observation and data from the (first) Sandia Fracture Challenge [1]. The geometry of the sample and its loading setup are reproduced in Fig. 29. Specifically, the specimen has a blunt notch A, three circular holes (B,C, and D), and two pins where loads $F$ are applied. To simplify the modeling of the pins, we assume perfect bonding between the specimen and the pins, eliminating the need to consider contact mechanics. We also assume that the pins share the same material properties as the specimen. The crack opening displacement (COD) can

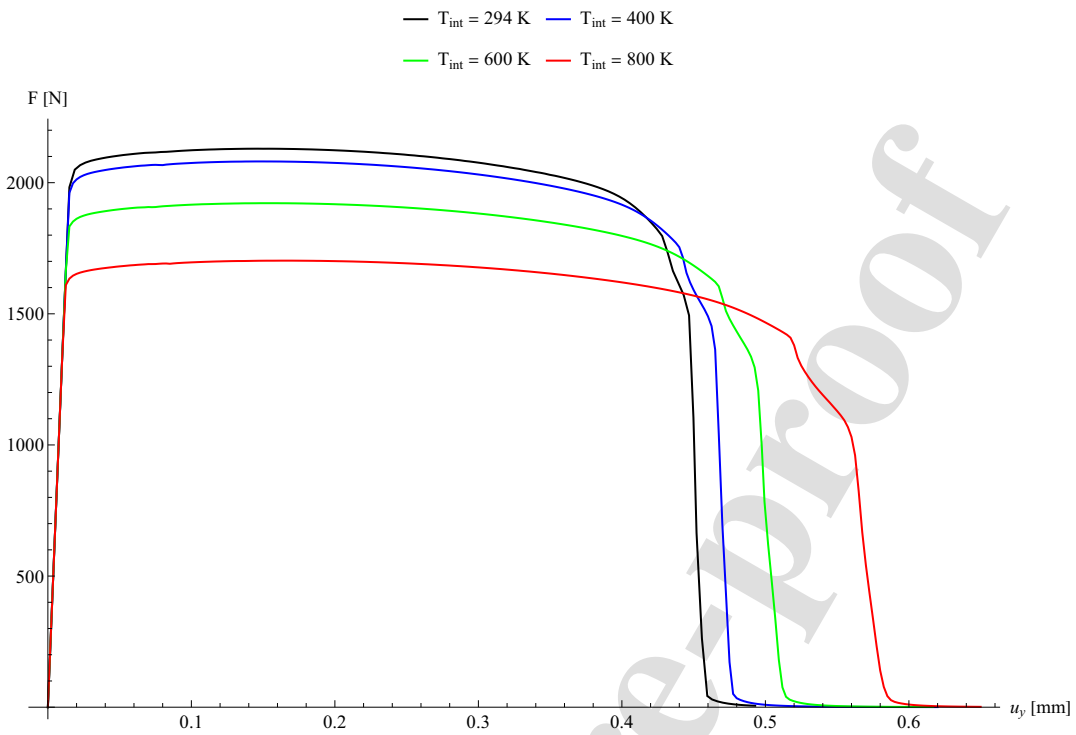


Figure 23: Effect of four different initial temperatures on the mechanical behavior of the I-shaped specimen, illustrated by the corresponding force-displacement curves. The loading rate is controlled by the prescribed velocity of $v_y = 10^{-3}$ mm/s.

be experimentally measured between two points located on opposite faces of the notch, as shown in Fig. 29.

Regarding the initial and boundary conditions, the sample is assumed to be undamaged with a uniformly distributed initial temperature of $T_{int} = 294$ K. The vertical velocity is prescribed as $v_y = 0.0127$ mm/s. Convective heat-transfer boundary conditions are imposed, as expressed in Eq. (79) with $h_q = 10^{-4}$ W/(mm$^2$K).

Compared to the previous examples, the major difference in this section is the adoption of the extended Johnson-Cook (XJC) plasticity model with nonlinear hardening behavior, introduced in Eq. (62), for the 15-5 PH alloy. Its material parameters are reported in Table 3, unless otherwise specified below. The length scale is chosen as $\ell_0 = 0.28$ mm, and the value of $g_f$ is set to 0.2. It is noteworthy that there are two additional material parameters (compared to the standard JC model): the saturation parameter $\delta$ and the ultimate stress $A^u$. Figs. 30 and 31 demonstrate the sensitivity of the force-COD curves to variations in $\delta$ and $A^u$, respectively. These studies highlight the effects of these additional material parameters of the XJC model on the load-bearing capacity. In general, these two parameters affect the rate at which the material response transitions gradually from the linear to the nonlinear regime. It is also observed that the model sensitivity to these two parameters is relatively small within the range of values considered here. For the remainder of this example, we use the values of $\delta = 6$ and $A^u = 1250$ MPa.

Additionally, we study the effect of the novel plastic degradation function, presented in Eq. (47), on failure behavior. To this end, we perform a sensitivity analysis with respect to the parameter $g_f$. Fig. 32 illustrates the influence of $g_f$ on the fracture process in terms of force-COD curves. It is observed that $g_f$ significantly affects the peak loads. Specifically, lower values of $g_f$ result in a more pronounced degradation of the yield stress, which leads to an earlier

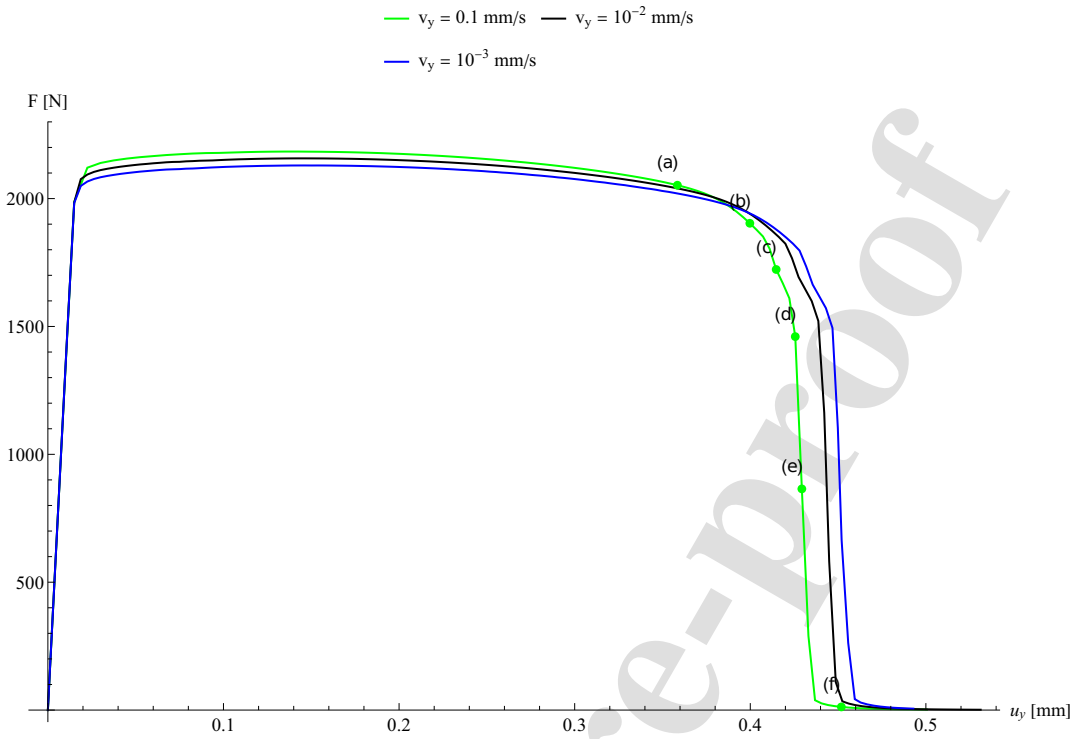


Figure 24: Effect of loading rates on the response of the I-shaped specimen, investigated using three different prescribed velocities. The initial temperature is assumed $T_{int} = 294$ K.

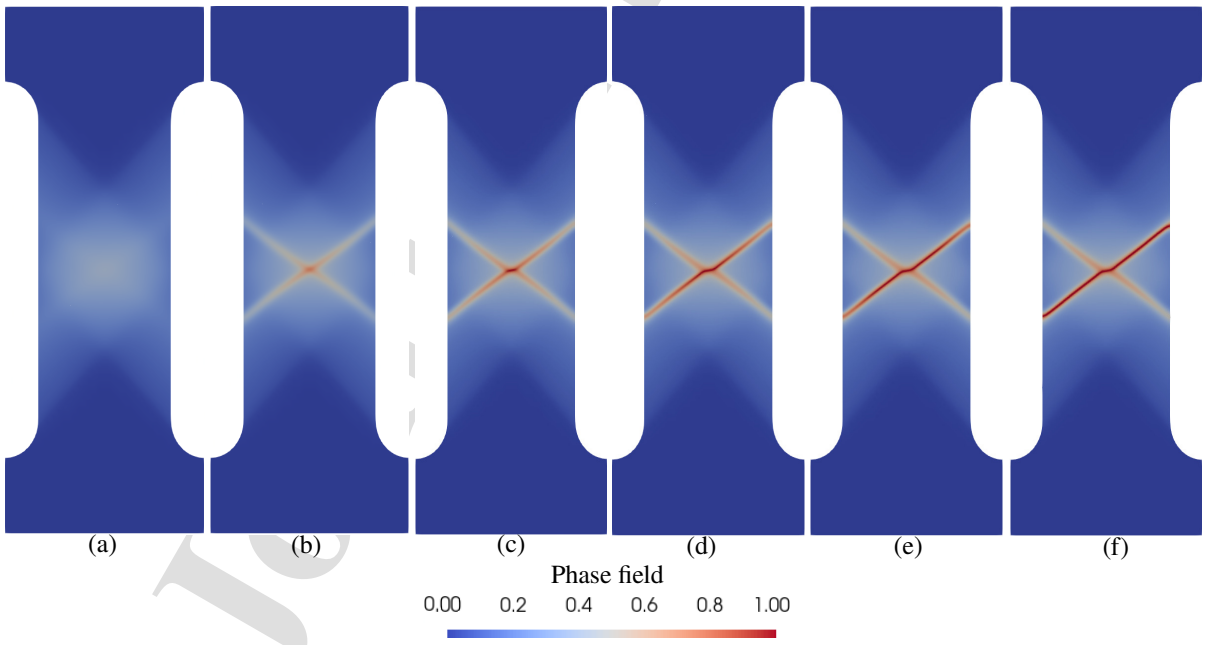


Figure 25: Snapshots showing the phase-field evolution at six time steps with vertical displacements $u_y$ of (a) 0.359 mm, (b) 0.400 mm, (c) 0.415 mm, (d) 0.426 mm, (e) 0.429 mm, and (f) 0.452 mm (as indicated by the corresponding letters in Fig. 24. The results are obtained with an initial temperature of $T_{int} = 294$ K and a loading rate imposed by the prescribed velocity of $v_y = 0.1$ mm/s.

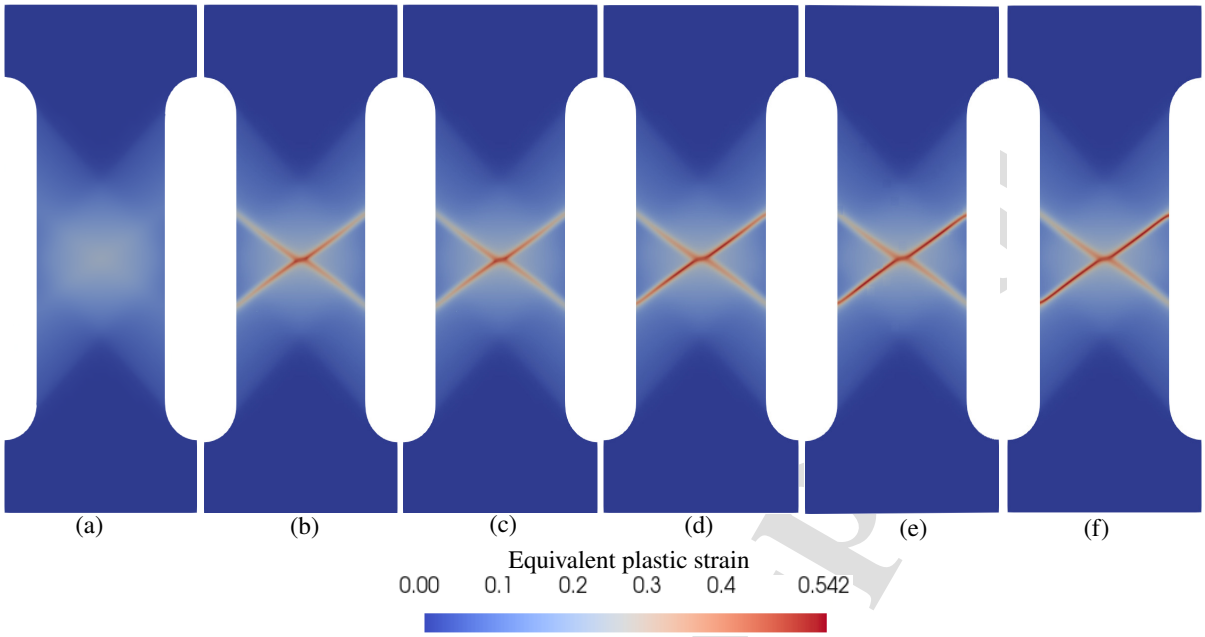


Figure 26: Snapshots showing the evolution of the equivalent plastic strain at six time steps with vertical displacements $u_y$ of (a) 0.359 mm, (b) 0.400 mm, (c) 0.415 mm, (d) 0.426 mm, (e) 0.429 mm, and (f) 0.452 mm (as indicated by the corresponding letters in Fig. 24. The results are obtained with an initial temperature of $T_{int} = 294$ K and a loading rate imposed by the prescribed velocity of $v_y = 0.1$ mm/s.

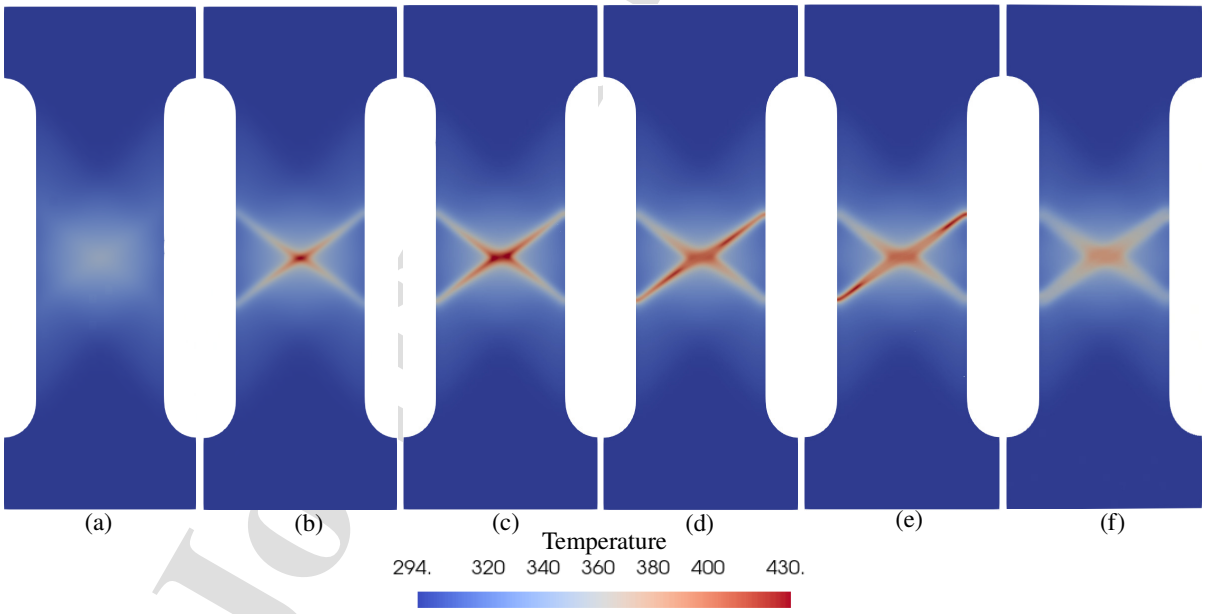


Figure 27: Snapshots showing the temperature evolution at six time steps with vertical displacements $u_y$ of (a) 0.359 mm, (b) 0.400 mm, (c) 0.415 mm, (d) 0.426 mm, (e) 0.429 mm, and (f) 0.452 mm (as indicated by the corresponding letters in Fig. 24. The results are obtained with an initial temperature of $T_{int} = 294$ K and a loading rate imposed by the prescribed velocity of $v_y = 0.1$ mm/s.

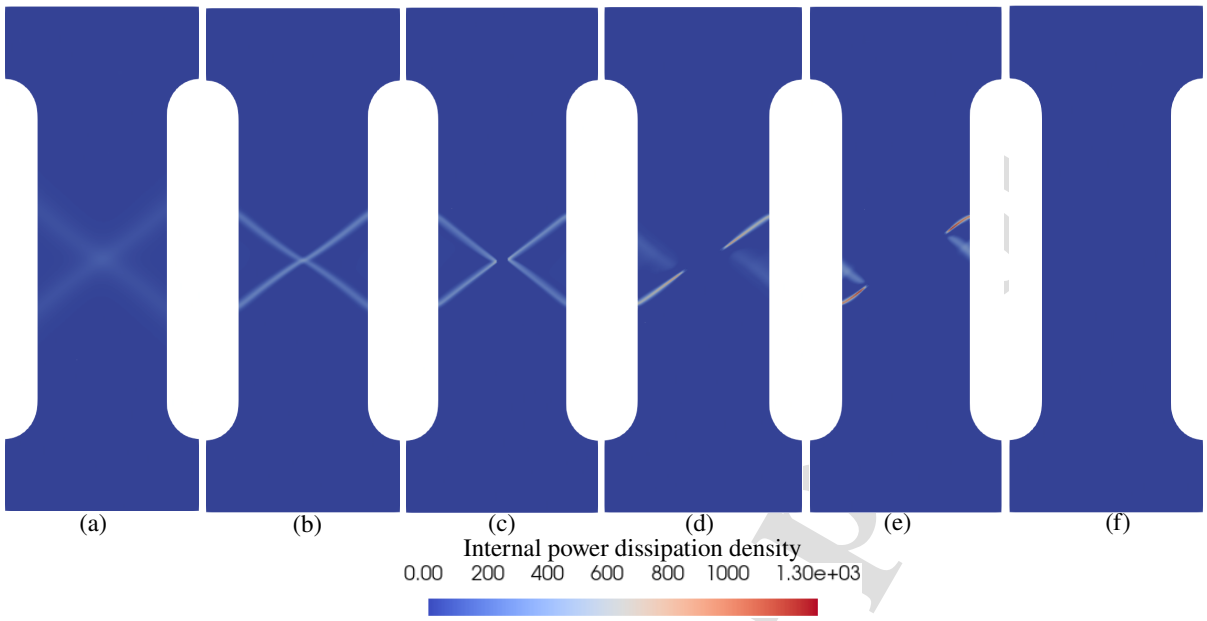


Figure 28: Snapshots showing the evolution of the internal power dissipation density at six time steps with vertical displacements $u_y$ of (a) 0.359 mm, (b) 0.400 mm, (c) 0.415 mm, (d) 0.426 mm, (e) 0.429 mm, and (f) 0.452 mm (as indicated by the corresponding letters in Fig. 24. The results are obtained with an initial temperature of $T_{int}$ = 294 K and a loading rate imposed by the prescribed velocity of $v_y$ = 0.1 mm/s.

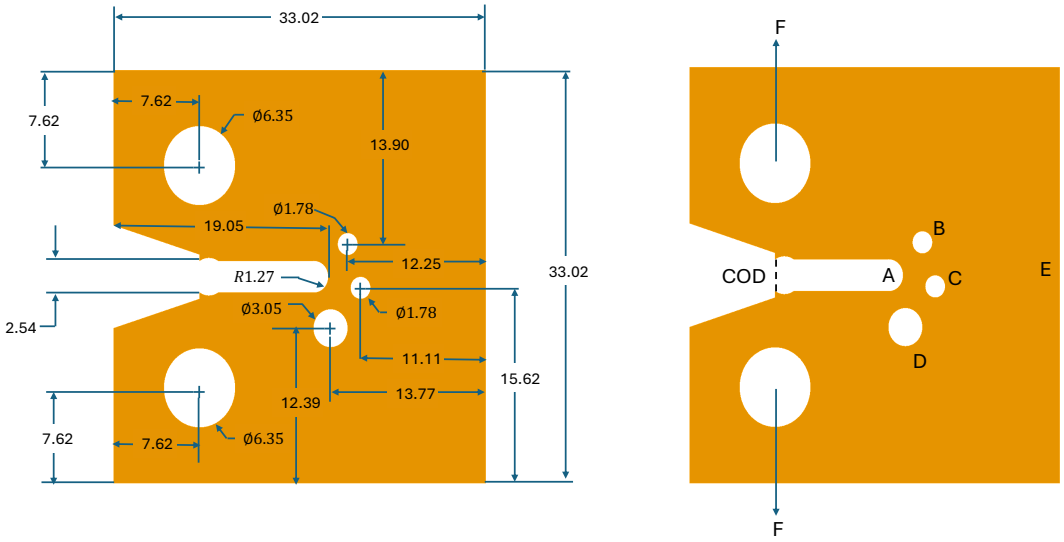


Figure 29: Geometry of the specimen in the Sandia Fracture Challenge from [1]: (left) dimensions (in millimeters) and (right) loading setup to measure crack opening displacements (COD).

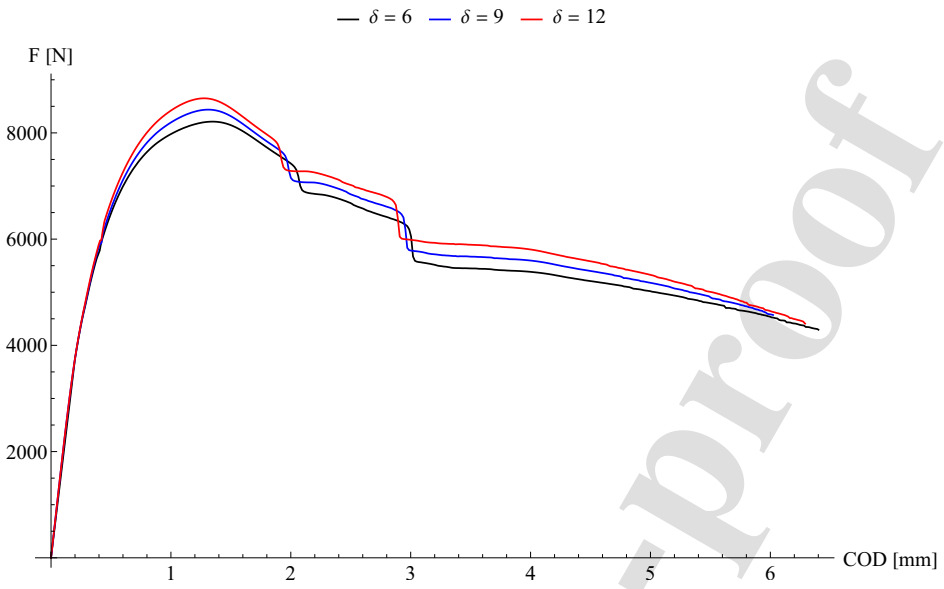


Figure 30: Sensitivity of the force-COD curves in the Sandia Fracture Challenge experiment [1] to variations in the values of the saturation parameter $\delta$ of the XJC model.

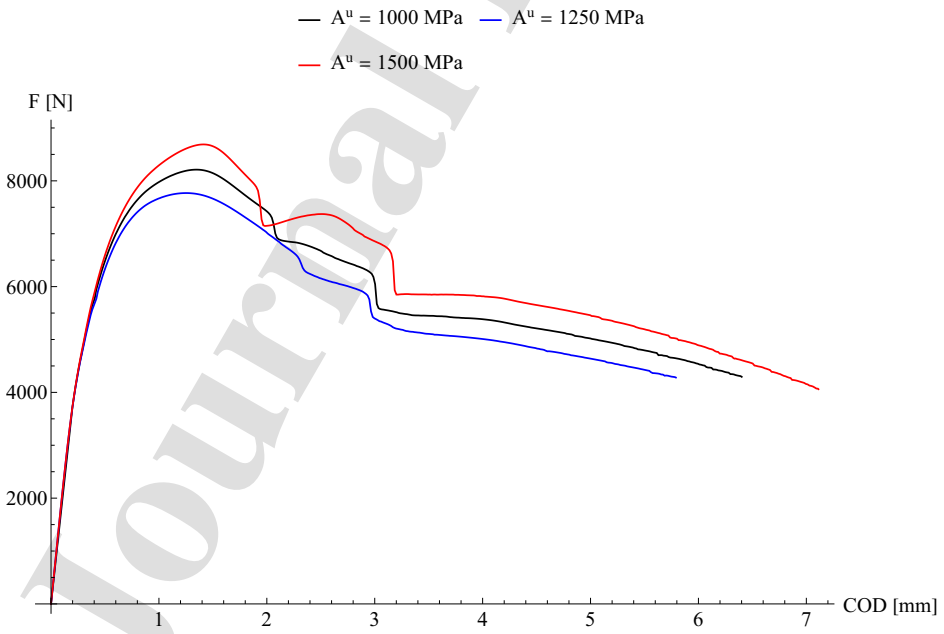


Figure 31: Sensitivity of the force-COD curves in the Sandia Fracture Challenge experiment [1] to variations in the values of the ultimate stress $A^u$ of the XJC model.

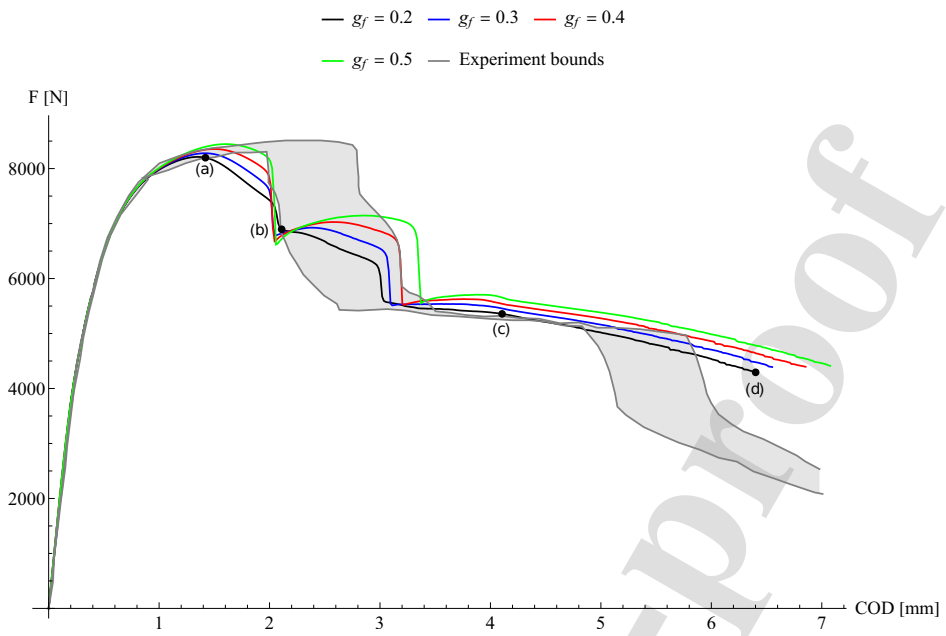


Figure 32: Sensitivity of the force-COD curves to variations in the values of $g_f$. Experimental data are reproduced from the Sandia Fracture Challenge in [1] (including lower and upper bounds as the boundaries of the shaded area). Good agreement between our current model (using the XJC model) and the experimental data is demonstrated.

reduction in the load-bearing capacity.

Fig. 32 also presents the force-COD curves for experimental data [1] (including lower and upper bounds as the boundary of the shaded area) and numerical results from the present work. These experimental data illustrate that the location of the three holes affects the critical crack paths, causing drops in load-bearing capacity (each associated with a crack connecting two holes). As a result, crack-arresting effects are observed due to the specific arrangement of the holes. Using our proposed framework, we capture the peak load and the gradual reduction in strength due to the holes. This simulation demonstrates very good agreement between our current model and the experimental data in terms of the force-COD curves.

Snapshots illustrating the critical crack path and plastic deformation are shown in Figs. 33 and 34 respectively. These figures focus on a specific region around the notch, including the three holes. We present the evolution of the phase-field variable (Fig. 33) and the equivalent plastic strain (Fig. 34) within this region of interest at four time steps with COD values of (a) 1.42 mm, (b) 2.11 mm, (c) 4.11 mm, and (d) 6.40 mm (as indicated by the same letters in Fig. 32). The corresponding loads for these time steps are 8.198 kN, 6.896 kN, 5.357 kN and 4.293 kN respectively. It is observed that the critical crack path develops on top of plastic localization zones. Specifically, it begins at notch A and sequentially connects holes D and C, extending towards the specimen's edge E, denoted by (A-D-C-E). (see Fig. 29). The aforementioned crack path is supported by experimental evidence in [1], as it represents one of the two observed crack paths, the other being (A-C-E).

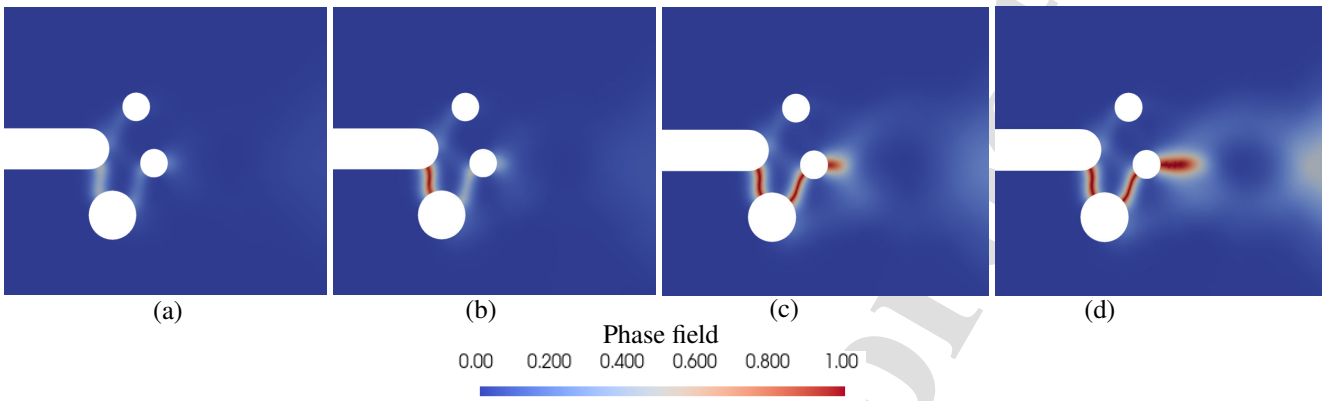


Figure 33: Snapshots illustrating the phase-field evolution at four time steps with vertical displacements $u_y$ of (a) 1.42 mm, (b) 2.11 mm, (c) 4.11 mm, and (d) 6.40 mm (as indicated by the same letters in Fig. 32).

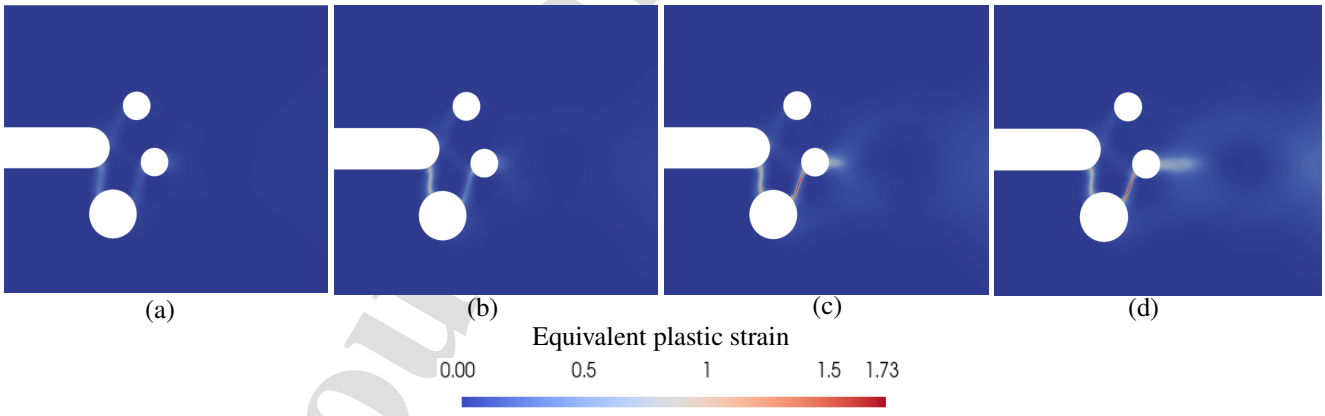


Figure 34: Snapshots illustrating the evolution of the equivalent plastic strain at four time steps with vertical displacements $u_y$ of (a) 1.42 mm, (b) 2.11 mm, (c) 4.11 mm, and (d) 6.40 mm (as indicated by the same letters in Fig. 32).

## 6. Conclusions

We developed a versatile phase-field framework for modeling ductile fracture within finite-strain elastoplasticity using a variational formulation of constitutive relations for generalized standard materials (GSMs). The variational structure of the proposed framework was characterized by a minimum principle for a functional that expresses the total power generation density, as the sum of power densities for reversible and irreversible processes. By minimizing this functional with a constraint on a (non-positive) von Mises yield function and applying the second law of thermodynamics, we determined the evolution equation for the equivalent plastic strain and the standard associative $J_2$ flow rule. This constrained optimization problem, arising from the minimum principle, was analytically solved for a broad class of temperature-dependent visco-plasticity models. In this particular class, the flow stress is multiplicatively decomposed into purely strain-hardening and thermal softening factors, along with a strain-rate hardening term.

The novel features of the phase-field fracture framework presented herein can be summarized as follows. We introduced

1. a cubic plastic degradation function to account for the gradual contribution of the stored plastic work to fracture, as well as the non-vanishing values of the damage-dependent yield stress,
2. closed-form expressions of the Helmholtz free energy and dissipation pseudo-potential for a wide class of visco-plasticity models (e.g., Johnson-Cook (JC) and a modified Zerilli-Armstrong (ZA) models),
3. an extended Johnson-Cook (XJC) plasticity model with a nonlinear hardening law,
4. a thermodynamically consistent form of the heating term due to plastic work, involving the plastic degradation function and the Taylor-Quinney (TQ) coefficient, for which we present a closed-form expression that depends on the plasticity model used.

The modeling capabilities of our phase-field (PF) framework were tested on four ductile fracture problems. These include three benchmark examples utilizing the Johnson-Cook (JC) plasticity model for X30Cr13 stainless steel, and one experimental test from the Sandia Fracture Challenge, which uses the novel XJC plasticity model for 15-5 PH alloy. The performance of the proposed PF framework was assessed by examining force-displacement curves, and by tracking the evolution of various fields, including phase field, equivalent plastic strain, and temperature, with the aid of contour plot snapshots. These studies focused on the interplay between thermomechanics and damage evolution. Based on all four examples, we arrive at the following conclusions.

- Plastic localization is a precursor to ductile fracture. In other words, damage accumulates most rapidly in shear bands where extensive plastic deformation takes place, such that cracks develop along a path that is congruent with these shear bands. This is observed in all of our computational results, but is especially worth noting in the Sandia Fracture Challenge problem, where our framework (with the XJC plasticity model) successfully reproduces the experimentally observed response and crack paths.

- The proposed plastic degradation function significantly affects ductility, with lower values of $g_f$ leading to loss of load-carrying capacity at an earlier stage of deformation. Tuning of this parameter may be needed to match experimental data. In addition, plastic work heating is affected by the plastic degradation function. Neglecting

such effects of damage on heat generation terms can lead to unrealistically high temperatures, especially in the vicinity of cracks.

- Higher initial temperatures reduce peak forces and delay the complete loss of load-bearing capacity. Conversely, higher loading rates increase peak forces but do not necessarily precipitate complete failure at an earlier stage of deformation. However, it is difficult to trace back individual aspects of the structural response to a particular physical process or mechanism. This is because the response of a structure stems from the complex interplay between various nonlinear, coupled processes at the level of each material point, in addition to geometric nonlinearities and local instabilities (such as shear bands) which can significantly affect global deformation and failure modes. This underscores the importance of accounting for the interplay between thermomechanics and damage, to the fullest possible extent, in computational frameworks for ductile fracture problems.

- In simulations using the JC plasticity model, we observe that the TQ coefficient is not highly sensitive to loading rate. To account for a stronger dependence of the TQ coefficient on the loading rate (in materials or conditions not considered herein), different plasticity models can be adopted by changing the stored energy density due to plastic work and the dissipation pseudo-potential. This can be achieved in a straightforward manner for a wide class of visco-plasticity models, owing to the modularity and versatility of the framework presented in this work.

In future work, we will focus our attention on developing specialized computational methods and/or machine learning techniques and we will explore their use in accelerating the solution of the system of coupled PDEs constituting the PF fracture framework presented here. We will also extend the framework to accommodate non-equilibrium thermodynamics, by introducing an additional state variable, referred to as the "equilibrium temperature" in [18]. This will allow phenomena driven by different thermodynamic processes to be represented more accurately (see also [19, 20]). Finally, we will calibrate this PF model, which captures fracture in multiphysics settings (including temperature-dependent visco-plastic effects), using experimental data with temperature measurements. This calibration will enhance its predictive capabilities in real-world applications, building upon foundational continuum damage approaches [73].

## Acknowledgments

Los Alamos National Laboratory is operated by Triad National Security, LLC, for the National Nuclear Security Administration of U.S. Department of Energy (Contract No. 89233218CNA000001).

## Appendix A. Details on kinematics in finite-strain elastoplasticity theory

In this appendix, we briefly present additional information on deformation tensors and stress measures in finite-strain elastoplasticity theory where multiplicative decomposition of the total deformation gradient and $J_2$ plasticity are assumed.

### *Appendix A.1. Deformation tensors*

First, deformation tensors are particularly essential for formulating the necessary constitutive laws at reference, intermediate, and spatial configurations (cf. Fig. 1). Starting from the reference configuration, the total and plastic right Cauchy-Green tensors are respectively given by

$$\left.\begin{aligned} \boldsymbol{C} &= \boldsymbol{F}^{\mathbf{T}}\boldsymbol{F} \\ \boldsymbol{C}^{p} &= \boldsymbol{F}^{p\mathbf{T}}\boldsymbol{F}^{p} \end{aligned}\right\}. \tag{A.1}$$

At the intermediate configuration, the elastic right Cauchy-Green tensor reads

$$\boldsymbol{\mathcal{C}}^{e} = \boldsymbol{F}^{e\mathbf{T}}\boldsymbol{F}^{e}\,, \tag{A.2}$$

while the viscoplastic velocity gradient is defined as follows

$$\boldsymbol{\mathcal{L}}^{\boldsymbol{p}} = \dot{\boldsymbol{F}}^{p}\boldsymbol{F}^{p\text{-}\mathbf{1}}\,. \tag{A.3}$$

At the spatial configuration, the total and elastic left Cauchy-Green tensors are respectively defined by

$$\left.\begin{aligned} \boldsymbol{b} &= \boldsymbol{F}\boldsymbol{F}^{\mathbf{T}} \\ \boldsymbol{b}^{e} &= \boldsymbol{F}^{e}\boldsymbol{F}^{e\mathbf{T}} \end{aligned}\right\}, \tag{A.4}$$

Regarding the deformation rates, the elastic and plastic velocity gradient tensors are given as follows

$$\left.\begin{aligned} \boldsymbol{l}^{e} &= \dot{\boldsymbol{F}}^{e}\boldsymbol{F}^{e\text{-}\mathbf{1}} \\ \boldsymbol{l}^{p} &= \boldsymbol{l} - \boldsymbol{l}^{e} = \boldsymbol{F}^{e}\boldsymbol{\mathcal{L}}^{\boldsymbol{p}}\boldsymbol{F}^{e\text{-}\mathbf{1}} \end{aligned}\right\}, \tag{A.5}$$

After some algebraic manipulation, we can show that additive decompositions of the rate of deformation and spin tensors hold as follows

$$\left.\begin{aligned} \boldsymbol{d} &= \boldsymbol{d}^{e} + \boldsymbol{d}^{p} \\ \widehat{\boldsymbol{w}} &= \widehat{\boldsymbol{w}}^{e} + \widehat{\boldsymbol{w}}^{p} \end{aligned}\right\}, \tag{A.6}$$

and one can derive the following kinematic relations

$$\left.\begin{aligned} \dot{\boldsymbol{\mathcal{C}}}^{e} &= 2\,\boldsymbol{F}^{e\mathbf{T}}\boldsymbol{d}^{e}\boldsymbol{F}^{e} \\ \dot{\boldsymbol{C}}^{p} &= 2\,\boldsymbol{F}^{p\mathbf{T}}\mathbf{sym}\left(\boldsymbol{\mathcal{L}}^{\boldsymbol{p}}\right)\boldsymbol{F}^{p} \end{aligned}\right\}. \tag{A.7}$$

These relations are particularly useful to transform rate quantities between configurations and objectively integrate flow rules [74].

*Appendix A.2. Constraints in $J_2$ flow rule*

In this work, the flow rule is expressed in terms of the spatial velocity gradient as follows

$$\boldsymbol{l}^p = \dot{\bar{\varepsilon}}_p \, \boldsymbol{n}^p \,, \tag{A.8}$$

where $\bar{\varepsilon}_p$ and $\boldsymbol{n}^p$ denote the unknown equivalent viscoplastic strain and the direction of viscoplastic flow respectively. In $J_2$ plasticity, the definition of the von Mises (equivalent) stress includes a factor of $\sqrt{3/2}$ to ensure that plastic flow occurs at the yield stress under uniaxial tension. In addition, the viscoplastic flow direction is normal to the yield surface in *stress space* and satisfies the following constraints [54]

$$\left.\begin{aligned} \mathrm{tr}\,(\boldsymbol{n}^p) &= 0 \\ \boldsymbol{n}^p : \boldsymbol{n}^p &= \frac{3}{2} \end{aligned}\right\} . \tag{A.9}$$

To complete the theory, an evolution equation for $\widehat{\boldsymbol{w}}^p$ is imposed so that the evolution of $\boldsymbol{l}^p$ in Eq. (A.8) is well-defined. We consider the specific constitutive assumption [74–77].

$$\widehat{\boldsymbol{w}}^p = \boldsymbol{0} \Leftrightarrow \boldsymbol{n}^p = \boldsymbol{n}^{p\mathbf{T}} \,. \tag{A.10}$$

Finally, we assume that the plastic flow is isochoric, and as a result

$$J^p = \det\left(\boldsymbol{F}^p\right) = 1 \Rightarrow J = J^e = \det\left(\boldsymbol{F}^e\right) \,. \tag{A.11}$$

After the aforementioned assumptions, the flow rule is simplified as follows

$$\boldsymbol{d}^p = \dot{\bar{\varepsilon}}_p \, \boldsymbol{n}^p \,. \tag{A.12}$$

*Appendix A.3. Stress measures*

In finite strain theory, the stress power can be equivalently expressed in the following forms

$$\boldsymbol{P} : \dot{\boldsymbol{F}} = \frac{1}{2} \boldsymbol{S} : \dot{\boldsymbol{C}} = \boldsymbol{\tau} : \boldsymbol{d} \,. \tag{A.13}$$

At the reference configuration, the second Piola-Kirchhoff stress is defined by

$$\boldsymbol{S} = \boldsymbol{F}^{-\mathbf{1}} \boldsymbol{P} \,, \tag{A.14}$$

where $\boldsymbol{P}$ represents the first Piola-Kirchhoff stress tensor.

At the spatial configuration, the Kirchhoff stress tensor is given by

$$\boldsymbol{\tau} = \boldsymbol{P} \boldsymbol{F}^{\mathbf{T}} \,. \tag{A.15}$$

where the deviator of the Kirchhoff stress tensor and the corresponding von Mises stress are defined

$$\left.\begin{aligned} \boldsymbol{s} &= \mathbf{dev}\,(\boldsymbol{\tau}) \\ s_v &= \sqrt{\frac{3}{2}} \|\boldsymbol{s}\| \end{aligned}\right\} . \tag{A.16}$$

Finally, at the intermediate configuration, the Mandel stress tensor is calculated by

$$\boldsymbol{\mathcal{M}} = \boldsymbol{F}^{e\mathbf{T}} \boldsymbol{P} \boldsymbol{F}^{p\mathbf{T}} \,. \tag{A.17}$$

## Appendix B. Steps in the Coleman-Noll procedure

In this appendix, we outline the steps of the Coleman-Noll procedure to derive thermodynamic restrictions on the constitutive relations. Interested readers are referred to [44, 54] for similar thermodynamic arguments.

The Clausius-Duhem form of the second law of thermodynamics in continuum mechanics postulates that entropy production is non-negative, as expressed as follows:

$$\rho_0 \dot{\eta} + \nabla_0 \cdot \left( \frac{\boldsymbol{Q}}{T} \right) \geq 0 \,. \tag{B.1}$$

It is common to recast the latter inequality in the following form

$$\mathbb{D} = \mathbb{D}^{int} + \mathbb{D}^{con} \geq 0 \,, \tag{B.2}$$

where the dissipation arising from heat conduction $\mathbb{D}^{con}$ and internal power dissipation density $\mathbb{D}^{int}$ are defined by

$$\left.\begin{aligned} \mathbb{D}^{con} &= -\frac{1}{T} \boldsymbol{Q} \cdot \nabla_0 T \\ \mathbb{D}^{int} &= \rho_0 T \dot{\eta} + \nabla_0 \cdot \boldsymbol{Q} \end{aligned}\right\} . \tag{B.3}$$

Combining Eqs. (10), (11) and (B.1) the second law of thermodynamics of our system reads

$$\mathbb{D} = \boldsymbol{\tau} : \boldsymbol{d} + \boldsymbol{\Xi} \cdot \nabla_0 \dot{d} + f_i \dot{d} - \rho_0 \dot{T} \eta - \rho_0 \dot{\psi} + \mathbb{D}^{con} \geq 0 \,. \tag{B.4}$$

Given the form of the free energy and its dependence on the state variables, the Helmholtz free energy rate can be expressed as

$$\dot{\psi} = \frac{\partial \psi}{\partial \boldsymbol{\mathcal{C}}^e} : \dot{\boldsymbol{\mathcal{C}}}^e + \frac{\partial \psi}{\partial d} \dot{d} + \frac{\partial \psi}{\partial \nabla_0 d} \cdot \nabla_0 \dot{d} + \frac{\partial \psi}{\partial T} \dot{T} + \frac{\partial \psi}{\partial \bar{\varepsilon}_p} \dot{\bar{\varepsilon}}_p \,. \tag{B.5}$$

Substituting the above equation into Eq. (B.4) and using Eq. (12) to simplify $\dot{T}$, the Clausius-Duhem inequality is reformulated into

$$\mathbb{D} = \left( \boldsymbol{\tau} - 2\rho_0 \boldsymbol{F}^e \frac{\partial \psi}{\partial \boldsymbol{\mathcal{C}}^e} \boldsymbol{F}^{e\mathbf{T}} \right) : \boldsymbol{d}^e + \left( \boldsymbol{\Xi} - \rho_0 \frac{\partial \psi}{\partial \nabla_0 d} \right) \cdot \nabla_0 \dot{d} + \left( f_i - \rho_0 \frac{\partial \psi}{\partial d} \right) \dot{d} + \left( \boldsymbol{\tau} : \boldsymbol{d}^p - \rho_0 \frac{\partial \psi}{\partial \bar{\varepsilon}_p} \dot{\bar{\varepsilon}}_p \right) + \mathbb{D}^{con} \geq 0 \,. \tag{B.6}$$

Assuming that the constitutive equation for the heat flux $\boldsymbol{Q}$ is chosen to satisfy

$$\mathbb{D}^{con} = -\frac{1}{T} \boldsymbol{Q} \cdot \nabla_0 T \geq 0, \tag{B.7}$$

the following inequality holds for the internal power dissipation density

$$\mathbb{D}^{int} = \mathbb{D} - \mathbb{D}^{con} = \left( \boldsymbol{\tau} : \boldsymbol{d}^p - \rho_0 \frac{\partial \psi}{\partial \bar{\varepsilon}_p} \dot{\bar{\varepsilon}}_p \right) \geq 0 \,. \tag{B.8}$$

This inequality can be expressed as follows

$$\mathbb{D}^{int} = \mathbb{D}^p - Y_s^p \dot{\bar{\varepsilon}}_p \geq 0 \,, \tag{B.9}$$

where $Y_s^p$ denotes the generalized thermodynamic force conjugate to $\dot{\bar{\varepsilon}}_p$ and the plastic dissipation is given by (p. 487 in [78])

$$\mathbb{D}^p = -\boldsymbol{P}^p : \dot{\boldsymbol{F}}^p = \boldsymbol{\mathcal{M}} : \boldsymbol{\mathcal{L}}^{\boldsymbol{p}} = \boldsymbol{\tau} : \boldsymbol{d}^p \,. \tag{B.10}$$

The simplified form of the internal power dissipation density in Eq. (19) is derived by substituting Eq. (7) into Eq. (B.8) and using Eq. (B.10).

**References**


[1] B. L. Boyce, S. L. Kramer, H. E. Fang, T. E. Cordova, M. K. Neilsen, K. Dion, A. K. Kaczmarowski, E. Karasz, L. Xue, A. J. Gross, et al., The sandia fracture challenge: blind round robin predictions of ductile tearing, International Journal of Fracture 186 (2014) 5–68.

[2] B. L. Boyce, S. L. Kramer, T. Bosiljevac, E. Corona, J. Moore, K. Elkhodary, C. Simha, B. W. Williams, A. R. Cerrone, A. Nonn, et al., The second sandia fracture challenge: predictions of ductile failure under quasi-static and moderate-rate dynamic loading, International Journal of Fracture 198 (2016) 5–100.

[3] S. L. Kramer, A. Jones, A. Mostafa, B. Ravaji, T. Tancogne-Dejean, C. C. Roth, M. G. Bandpay, K. Pack, J. T. Foster, M. Behzadinasab, et al., The third sandia fracture challenge: predictions of ductile fracture in additively manufactured metal, International Journal of Fracture 218 (2019) 5–61.

[4] G. Barrow, Review of experimental and theoretical techniques for assessing cutting temperatures, CIRP, l 973, 22,(2), 203-2 ll (1974).

[5] D. Rittel, L. Zhang, S. Osovski, The dependence of the Taylor–Quinney coefficient on the dynamic loading mode, Journal of the Mechanics and Physics of Solids 107 (2017) 96–114.

[6] G. R. Johnson, W. H. Cook, Fracture characteristics of three metals subjected to various strains, strain rates, temperatures and pressures, Engineering fracture mechanics 21 (1985) 31–48.

[7] D. Steinberg, C. Lund, A constitutive model for strain rates from 10- 4 to 106 s-, Journal of applied physics 65 (1989) 1528–1533.

[8] F. J. Zerilli, R. W. Armstrong, Dislocation-mechanics-based constitutive relations for material dynamics calculations, Journal of applied physics 61 (1987) 1816–1825.

[9] D. L. Preston, D. L. Tonks, D. C. Wallace, Model of plastic deformation for extreme loading conditions, Journal of applied physics 93 (2003) 211–220.

[10] H. M. Mourad, C. A. Bronkhorst, F. L. Addessio, C. M. Cady, D. W. Brown, S. R. Chen, G. T. Gray, Incrementally objective implicit integration of hypoelastic–viscoplastic constitutive equations based on the mechanical threshold strength model, Computational Mechanics 53 (2014) 941–955.

[11] B. Halphen, Q. S. Nguyen, Sur les matériaux standard généralisés, Journal de mécanique 14 (1975) 39–63.

[12] M. Ortiz, L. Stainier, The variational formulation of viscoplastic constitutive updates, Computer methods in applied mechanics and engineering 171 (1999) 419–444.

[13] C. Comi, A. Corigliano, G. Maier, Extremum properties of finite-step solutions in elastoplasticity with nonlinear mixed hardening, International journal of solids and structures 27 (1991) 965–981.

[14] H. Ziegler, C. Wehrli, The derivation of constitutive relations from the free energy and the dissipation function, in: Advances in applied mechanics, volume 25, Elsevier, 1987, pp. 183–238.

[15] A. Mielke, A Mathematical Framework for Generalized Standard Materials in the Rate-Independent Case, Springer Berlin Heidelberg, Berlin, Heidelberg, 2006, pp. 399–428. doi:10.1007/978-3-540-34961-7_12.

[16] M. Canadija, J. Mosler, On the thermomechanical coupling in finite strain plasticity theory with non-linear kinematic hardening by means of incremental energy minimization, International Journal of Solids and Structures 48 (2011) 1120–1129.

[17] K. Hackl, Generalized standard media and variational principles in classical and finite strain elastoplasticity, Journal of the Mechanics and Physics of Solids 45 (1997) 667–688.

[18] Q. Yang, L. Stainier, M. Ortiz, A variational formulation of the coupled thermo-mechanical boundary-value problem for general dissipative solids, Journal of the Mechanics and Physics of Solids 54 (2006) 401–424.

[19] L. Stainier, A variational approach to modeling coupled thermo-mechanical nonlinear dissipative behaviors, in: Advances in Applied Mechanics, volume 46, Elsevier, 2013, pp. 69–126.

[20] T. Heuzé, L. Stainier, A variational formulation of thermomechanical constitutive update for hyperbolic conservation laws, Computer Methods in Applied Mechanics and Engineering 394 (2022) 114893.

[21] A. A. Griffith, Vi. the phenomena of rupture and flow in solids, Philosophical transactions of the royal society of london. Series A, containing papers of a mathematical or physical character 221 (1921) 163–198.

[22] A. A. Griffith, Theory of rupture, in: Proc. 1st. Int. Cong. Appl. Mech., Delft, 1924, pp. 55–63.

[23] J.-Y. Wu, V. P. Nguyen, C. T. Nguyen, D. Sutula, S. Sinaie, S. P. Bordas, Phase-field modeling of fracture, Advances in applied mechanics 53 (2020) 1–183.

[24] G. Irwin, Fracture dynamics, fracturing of metals. american society of metals, Cleveland, Ohio (1948) 296.

[25] E. Orowan, Fracture and strength of solids, Reports on progress in physics 12 (1949) 185.

[26] F. Erdogan, Fracture mechanics, International Journal of Solids and Structures 37 (2000) 171–183. doi:https://doi.org/10.1016/S0020-7683(99)00086-4.

[27] B. Bourdin, G. A. Francfort, J.-J. Marigo, Numerical experiments in revisited brittle fracture, Journal of the Mechanics and Physics of Solids 48 (2000) 797–826.

[28] G. A. Francfort, J. J. Marigo, Revisiting brittle fracture as an energy minimization problem, Journal of the Mechanics and Physics of Solids 46 (1998) 1319–1342.

[29] L. Svolos, H. M. Mourad, G. Manzini, K. Garikipati, A fourth-order phase-field fracture model: Formulation and numerical solution using a continuous/discontinuous Galerkin method, Journal of the Mechanics and Physics of Solids 165 (2022) 104910.

[30] R. de Borst, C. V. Verhoosel, Gradient damage vs phase-field approaches for fracture: Similarities and differences, Computer Methods in Applied Mechanics and Engineering 312 (2016) 78–94.

[31] G. N. Wells, K. Garikipati, L. Molari, A discontinuous galerkin formulation for a strain gradient-dependent damage model, Computer Methods in Applied Mechanics and Engineering 193 (2004) 3633–3645.

[32] L. Molari, G. N. Wells, K. Garikipati, F. Ubertini, A discontinuous galerkin method for strain gradient-dependent damage: study of interpolations and convergence, Computer Methods in Applied Mechanics and Engineering 195 (2006) 1480–1498.

[33] S. Rudraraju, A. Salvi, K. Garikipati, A. M. Waas, Predictions of crack propagation using a variational multiscale approach and its application to fracture in laminated fiber reinforced composites, Composite structures 94 (2012) 3336–3346.

[34] C. Miehe, F. Welschinger, M. Hofacker, Thermodynamically consistent phase-field models of fracture: Variational principles and multi-field FE implementations, International journal for numerical methods in engineering 83 (2010) 1273–1311.

[35] M. J. Borden, C. V. Verhoosel, M. A. Scott, T. J. Hughes, C. M. Landis, A phase-field description of dynamic brittle fracture, Computer Methods in Applied Mechanics and Engineering 217 (2012) 77–95.

[36] A. Schlüter, A. Willenbücher, C. Kuhn, R. Müller, Phase field approximation of dynamic brittle fracture, Computational Mechanics 54 (2014) 1141–1161.

[37] B. Bourdin, G. A. Francfort, J.-J. Marigo, The variational approach to fracture, Journal of elasticity 91 (2008) 5–148.

[38] C. V. Verhoosel, R. de Borst, A phase-field model for cohesive fracture, International Journal for numerical methods in Engineering 96 (2013) 43–62.

[39] J. Vignollet, S. May, R. De Borst, C. V. Verhoosel, Phase-field models for brittle and cohesive fracture, Meccanica 49 (2014) 2587–2601.

[40] H. Ulmer, M. Hofacker, C. Miehe, Phase field modeling of brittle and ductile fracture, Pamm 13 (2013) 533–536.

[41] C. Miehe, F. Aldakheel, A. Raina, Phase field modeling of ductile fracture at finite strains: A variational gradient-extended plasticity-damage theory, International Journal of Plasticity 84 (2016) 1–32.

[42] M. J. Borden, T. J. R. Hughes, C. M. Landis, A. Anvari, I. J. Lee, A phase-field formulation for fracture in ductile materials: Finite deformation balance law derivation, plastic degradation, and stress triaxiality effects, Computer Methods in Applied Mechanics and Engineering 312 (2016) 130–166. doi:10.1016/j.cma.2016.09.005.

[43] M. Ambati, T. Gerasimov, L. De Lorenzis, Phase-field modeling of ductile fracture, Computational Mechanics 55 (2015) 1017–1040.

[44] C. McAuliffe, H. Waisman, A unified model for metal failure capturing shear banding and fracture, International Journal of Plasticity 65 (2015) 131–151.

[45] H. Zhang, X.-Y. Pei, H. Peng, J.-Y. Wu, Phase-field modeling of spontaneous shear bands in collapsing thick-walled cylinders, Engineering Fracture Mechanics 249 (2021) 107706.

[46] H. Badnava, M. A. Msekh, E. Etemadi, T. Rabczuk, An h-adaptive thermo-mechanical phase field model for fracture, Finite Elements in Analysis and Design 138 (2018) 31–47.

[47] C. Yan, X. Wang, D. Huang, G. Wang, A new 3D continuous-discontinuous heat conduction model and coupled thermomechanical model for simulating the thermal cracking of brittle materials, International Journal of Solids and Structures 229 (2021) 111123.

[48] M. Dittmann, F. Aldakheel, J. Schulte, F. Schmidt, M. Krüger, P. Wriggers, C. Hesch, Phase-field modeling of porous-ductile fracture in non-linear thermo-elasto-plastic solids, Computer Methods in Applied Mechanics and Engineering 361 (2020) 112730.

[49] L. Svolos, H. M. Mourad, C. A. Bronkhorst, H. Waisman, Anisotropic thermal-conductivity degradation in the phase-field method accounting for crack directionality, Engineering Fracture Mechanics 245 (2021) 107554.

[50] E. H. Lee, Elastic-plastic deformation at finite strains, Journal of Applied Mechanics (1969).

[51] J. C. Simo, T. J. Hughes, Computational inelasticity, volume 7, Springer Science & Business Media, 2006.

[52] T. Belytschko, W. K. Liu, B. Moran, K. Elkhodary, Nonlinear finite elements for continua and structures, John wiley & sons, 2014.

[53] P. Wriggers, Nonlinear finite element methods, Springer Science & Business Media, 2008.

[54] B. Talamini, M. R. Tupek, A. J. Stershic, T. Hu, J. W. Foulk III, J. T. Ostien, J. E. Dolbow, Attaining regularization length insensitivity in phase-field models of ductile failure, Computer Methods in Applied Mechanics and Engineering 384 (2021) 113936.

[55] M. J. Borden, T. J. Hughes, C. M. Landis, A. Anvari, I. J. Lee, A phase-field formulation for fracture in ductile materials: Finite deformation balance law derivation, plastic degradation, and stress triaxiality effects, Computer Methods in Applied Mechanics and Engineering 312 (2016) 130–166.

[56] R. Zaera, J. Fernández-Sáez, An implicit consistent algorithm for the integration of thermoviscoplastic constitutive equations in adiabatic conditions and finite deformations, International journal of solids and structures 43 (2006) 1594–1612.

[57] C. Miehe, M. Hofacker, L. M. Schänzel, F. Aldakheel, Phase field modeling of fracture in multi-physics problems. Part II. Coupled brittle-to-ductile failure criteria and crack propagation in thermo-elastic–plastic solids, Computer Methods in Applied Mechanics and Engineering 294 (2015) 486–522. doi:10.1016/j.cma.2014.11.017.

[58] H. Amor, J.-J. Marigo, C. Maurini, Regularized formulation of the variational brittle fracture with unilateral contact: Numerical experiments, Journal of the Mechanics and Physics of Solids 57 (2009) 1209–1229.

[59] N. Ranc, A. Chrysochoos, Calorimetric consequences of thermal softening in johnson–cook's model, Mechanics of Materials 65 (2013) 44–55.

[60] H. Montazer Hojjat, S. Kozinov, D. Balzani, An a priori irreversible phase-field formulation for ductile fracture at finite strains based on the allen–cahn theory: a variational approach and fe-implementation, Archive of Applied Mechanics 94 (2024) 365–390.

[61] M. Ambati, R. Kruse, L. De Lorenzis, A phase-field model for ductile fracture at finite strains and its experimental verification, Computational Mechanics 57 (2016) 149–167.

[62] Y. Lin, X.-M. Chen, A combined johnson–cook and zerilli–armstrong model for hot compressed typical high-strength alloy steel, Computational Materials Science 49 (2010) 628–633.

[63] L. Svolos, C. A. Bronkhorst, H. Waisman, Thermal-conductivity degradation across cracks in coupled thermo-mechanical systems modeled by the phase-field fracture method, Journal of the Mechanics and Physics of Solids 137 (2020) 103861.

[64] G. Giudicelli, A. Lindsay, L. Harbour, C. Icenhour, M. Li, J. E. Hansel, P. German, P. Behne, O. Marin, R. H. Stogner, J. M. Miller, D. Schwen, Y. Wang, L. Munday, S. Schunert, B. W. Spencer, D. Yushu, A. Recuero, Z. M. Prince, M. Nezdyur, T. Hu, Y. Miao, Y. S. Jung, C. Matthews, A. Novak, B. Langley, T. Truster, N. Nobre, B. Alger, D. Andrš, F. Kong, R. Carlsen, A. E. Slaughter, J. W. Peterson, D. Gaston, C. Permann, 3.0 - MOOSE: Enabling massively parallel multiphysics simulations, SoftwareX 26 (2024) 101690. doi:https://doi.org/10.1016/j.softx.2024.101690.

[65] L. Svolos, J. N. Plohr, G. Manzini, H. M. Mourad, On the convexity of phase-field fracture formulations: Analytical study and comparison of various degradation functions, International Journal of Non-Linear Mechanics 150 (2023) 104359.

[66] T. Jin, Z. Li, K. Chen, A novel phase-field monolithic scheme for brittle crack propagation based on the limited-memory bfgs method with adaptive mesh refinement, International Journal for Numerical Methods in Engineering 125 (2024) e7572.

[67] T. D. Blacker, W. J. Bohnhoff, T. L. Edwards, CUBIT mesh generation environment. Volume 1: Users manual, Technical Report, Sandia National Lab.(SNL-NM), Albuquerque, NM (United States), 1994.

[68] A. Gupta, U. M. Krishnan, T. K. Mandal, R. Chowdhury, V. P. Nguyen, An adaptive mesh refinement algorithm for phase-field fracture models: Application to brittle, cohesive, and dynamic fracture, Computer Methods in Applied Mechanics and Engineering 399 (2022) 115347.

[69] D. Schneider, B. Nestler, et al., Realization of adaptive mesh refinement for phase-field model of thermal fracture within the fenics framework, Engineering Fracture Mechanics 293 (2023) 109676.

[70] J. Mediavilla, R. Peerlings, M. Geers, Discrete crack modelling of ductile fracture driven by non-local softening plasticity, International journal for numerical methods in engineering 66 (2006) 661–688.

[71] F. Aldakheel, P. Wriggers, C. Miehe, A modified gurson-type plasticity model at finite strains: formulation, numerical analysis and phase-field coupling, Computational Mechanics 62 (2018) 815–833.

[72] P. Verleysen, J. Peirs, Quasi-static and high strain rate fracture behaviour of ti6al4v, International Journal of Impact Engineering 108 (2017) 370–388.

[73] K. Pack, M. Luo, T. Wierzbicki, Sandia fracture challenge: blind prediction and full calibration to enhance fracture predictability, International Journal of Fracture 186 (2014) 155–175.

[74] J. Simo, Handbook of numerical analysis vi; chapter numerical analysis and simulation of plasticity, 1998.

[75] Y. F. Dafalias, The plastic spin concept and a simple illustration of its role in finite plastic transformations, Mechanics of Materials 3 (1984) 223–233.

[76] Y. F. Dafalias, The Plastic Spin, Journal of Applied Mechanics 52 (1985) 865–871. doi:10.1115/1.3169160.

[77] E. A. de Souza Neto, D. Peric, D. R. Owen, Computational methods for plasticity: theory and applications, John Wiley & Sons, 2011.

[78] J. Lubliner, Plasticity theory, Courier Corporation, 2008.

- A phase-field fracture framework for rate- and temperature-dependent materials.
- A wide class of plasticity models for generalized standard materials is considered.
- Novel closed-form expressions for the plastic degradation function and dissipation.
- Benchmark problems and data used to assess performance and predictive capability.
- An extended Johnson-Cook plasticity model used to reproduce experimental data.

**Declaration of interests**

☒ The authors declare that they have no known competing financial interests or personal relationships that could have appeared to influence the work reported in this paper.

☐ The authors declare the following financial interests/personal relationships which may be considered as potential competing interests: